

Solvation effects on halides core spectra with Multilevel Real-Time quantum embedding

Jessica A. Martinez B.,[†] Matteo De Santis,[‡] Michele Pavanello,^{¶,§} Valérie
Vallet,[‡] and André Severo Pereira Gomes^{*,‡}

[†]*Department of Chemistry, Rutgers University, Newark, New Jersey*

[‡]*Univ. Lille, CNRS, UMR 8523 - PhLAM - Physique des Lasers Atomes et Molécules,
F-59000 Lille, France*

[¶]*Department of Physics, Rutgers University, Newark, New Jersey*

[§]*Department of Chemistry, Rutgers University, Newark, New Jersey*

E-mail: andre.gomes@univ-lille.fr

Abstract

Quantum embedding techniques are gaining popularity as they provide an accurate description of electronic systems at a reduced computational cost. In this work, we introduce a novel subsystem-based electronic structure embedding method that combines the projection-based block-orthogonalized Manby-Miller embedding (BOMME) with the density-based Frozen Density Embedding (FDE) methods. Our approach is especially effective for systems in which the building blocks (or subsystems) interact at varying strengths while still maintaining a lower computational cost compared to a quantum simulation of the entire system. To evaluate the performance of our method, we assess its ability to reproduce the X-ray absorption spectra (XAS) of chloride and fluoride anions in aqueous solutions (based on a 50-water droplet model) via real-time time-dependent density functional theory (rt-TDDFT) calculations. We employ an

ensemble approach to compute XAS for the K and L_1 edges, utilizing multiple snapshots of configuration space obtained from classical molecular dynamics simulations with a polarizable force field. Configurational averaging influences both the broadening of spectral features and their intensities, with contributions to the final intensities originating from different geometry configurations. We found that embedding models that are too approximate for halide-water specific interactions, as in the case of FDE, fail to reproduce the experimental spectrum for chloride. Meanwhile, the BOMME approach tends to overestimate intensities, particularly for higher energy features because of finite-size effects. Combining FDE for the second solvation shell and retaining BOMME for the first solvation shell mitigates this effect, resulting in an overall improved agreement within the energy range of the experimental spectrum. Additionally, we compute the transition densities of the relevant transitions, confirming that these transitions occur within the halide systems. Thus, our real-time QM/QM/QM embedding method proves to be a promising approach for modeling XAS of solvated systems.

1 Introduction

The aqueous dynamics of anions such as halides and other halogenated species have attracted the interest of many scientists eager to uncover their multiple electronic processes.¹⁻⁵ These processes depend both on the intrinsic characteristics of the ions themselves and their interaction with the surrounding hydration shells.⁶⁻⁹ Particularly noteworthy is the strong influence on the extended structure of water resulting from the short-range interactions between ions and their surrounding waters.^{7,10} Ion solvation effects underpin the development of innovative technologies such as rechargeable fluoride-ion batteries¹¹ and capacitive deionization electrodes (CDI).¹² For the latter, it has been demonstrated that the local distribution of the hydrogen bond network created by the anion directly retards the dielectric response of the CDI electrode.

Among the methods that can be used to characterize the behavior of solvated ions, those

probing core electrons, such as X-ray absorption spectroscopy (XAS), are particularly well-suited to get an insight into the structural and electronic behavior of anionic systems, due to the great sensitivity of core states to even the slightest perturbations in the electronic structure of the absorbing center (such as those provoked by changes in their local environment).^{7,13} Interpreting XAS experiments is challenging due to the myriad physical processes at play, necessitating theoretical models to make sense of experimental observations.

Among theoretical approaches, effective theories (e.g. crystal or ligand-field models, impurity models, etc) are widely used^{14,15} as they efficiently account for environment, electron correlation, and relativistic effects, offering a cost-effective way to simulate X-ray absorption near edge structure (XANES) and long-range multiple scattering (EXAFS) regions.^{16,17} Both techniques have been used to simulate the spectra of aqueous iodide, bromide, and chloride.⁷ A alternative flexible method for simulating XANES is found in molecular electronic structure methods and among them those based on time-dependent density functional theory employing the restricted energy window formalism (REW-TDDFT,¹⁸ referred to hereafter as TDDFT), due to their favorable balance between computational cost and accuracy. While TD-DFT is known to underestimate the absolute value of absorption energies due to the lack of core hole relaxation,^{19,20} experimental spectral features can be accurately reproduced once a global shift is applied^{21,22} to the features of the edge under consideration.

Standard TDDFT calculations, however, can be computationally expensive for large-scale systems involving a solute accompanied by tens to hundreds of solvent molecules, especially when temperature effects are taken into account via molecular dynamics calculations. In such cases, embedding approaches prove useful in reducing computational costs by allowing the tailoring of accuracy for different parts of the system (subsystems) based on their importance to the property of interest.

The use of a classical representation for the solvent and solvent-solute interactions, as done in widely popular approaches such as QM/MM (quantum mechanics/molecular mechanics) model^{2,23} or the quasi-chemical theory (QCT) with polarizable continuum model

(PCM),²⁴ brings about substantial computational savings. However, it may potentially miss effects due the quantum mechanical nature of the solvent and, in the case of PCM, struggle to capture directional interactions like hydrogen bonds.²⁵ These shortcomings can be alleviated by extending the QM-level region to include a number of solvent molecules, though this approach does not guarantee a quick convergence of calculated spectra with the number of explicit solvent molecules.²⁶

Purely quantum embedding (QE) techniques^{27–30} have emerged more recently, with the aim to retain a fully quantum mechanical description for all subsystems. In approaches such as the frozen density embedding (FDE)^{29,31–34} method, the aim is to represent the interaction between subsystems by a (local) embedding potential constructed from subsystem electron densities. This allows for linear scaling calculations with respect to the number of subsystems,^{31,35} as well as for very straightforward combinations of electronic structure methods (wavefunction-based, DFT-based, etc) for the computation of valence³⁶ and core³⁷ ionizations and excitations.^{19,38} However, despite being a formally exact theory, in practical applications, FDE faces difficulties to describe situations in which a system is partitioned into strongly interacting subsystems, primarily due to the use of approximations to the kinetic energy density functional.

Apart from standard response theory, FDE has also been used in combination with real-time TDDFT (rt-TDDFT) to obtain valence^{39,40} and core excited states,⁴¹ though for discrete systems the response of the environment has, to date, been disregarded, preventing the description of the coupling of the response of all subsystems. In the context of condensed matter systems, subsystem couplings at rt-TDDFT have been taken into account, see Ref. [31].

In other QE approaches based on projection techniques, the difficulties in partitioning strongly interacting subsystems are effectively circumvented. One such technique, the Block-Orthogonalized Manby-Miller embedding (BOMME) method,²⁷ offers the advantage of dividing a system into two domains. The active region (Domain A) is treated with a

high-level (mean-field) theory, while the remainder of the systems, taken to be the environment (Domain B), is treated with a lower level (mean-field) theory. BOMME shows promise in reducing computational cost for standard electronic structure implementations that capture valence excited state energies for both intermolecular and intramolecular embedding schemes.⁴² Beyond ground-state properties, BOMME has been used to investigate valence⁴³ and core⁴¹ excited states in combination with rt-TDDFT, and shown to be able to capture the coupling between the response of the different domains. However, these applications remain limited to molecular systems or clusters of small to moderate size, as with other projection-based approaches, the need to define basis functions spanning the whole system introduces a higher computational cost with respect to FDE.

In this work, we combine the strengths of BOMME (effective at capturing strong inter and intramolecular interactions) and FDE (efficient in including long-range interactions in large-scale systems) to accelerate real-time TDDFT calculations of core excited states, in what we shall refer to as multilevel rt-TDDFT quantum embedding. We will showcase this approach by carrying out simulations of the K-edge spectra of hydrated chloride and fluoride anions, as well as the L₁-edge spectra of hydrated chloride, complementing our prior work on valence³⁶ and core³⁷ ionizations. In the case of chloride experimental K-edge spectra are available,⁷ together with TDDFT calculations on static structures where between 6 to 8 molecules surrounding the ion have been considered, each exhibiting a distinct spectral profile. Our first goal in this paper will be to revisit this question and assess how more sophisticated models compare to experimental results.

The manuscript is organized as follows: First, we provide a comprehensive review of the theoretical background, encompassing the formalism of rt-TDDFT, the theories of frozen density embedding and Block-Orthogonalized Manby-Miller embedding, along with their rt-TDDFT extensions, and their combination with the Multilevel embedding method presented here. Secondly, we discuss implementation details that enabled more efficient rt-TDDFT-FDE calculations. Thirdly, we present and thoroughly discuss our results obtained with

different embedding methods, for the aqueous chloride and fluoride. Finally, we offer concluding remarks and outline potential avenues for further research.

2 Theoretical Background

Ground-state density functional theory (DFT) is governed by the Kohn-Sham (KS) equations expressed in atomic units as follows:

$$\left(-\frac{\nabla_i^2}{2} + v_{\text{eff}}[\rho](\mathbf{r})\right)\psi_i(\mathbf{r}) = \epsilon_i\psi_i(\mathbf{r}). \quad (1)$$

In the above equation, we define the KS orbitals, $\psi_i(\mathbf{r})$, and the KS orbital energies, ϵ_i .

Time-dependent DFT, instead, is defined by the time-dependent KS equations which yield the time-dependent KS orbitals. Namely,

$$\left(-\frac{\nabla_i^2}{2} + v_{\text{eff}}(\mathbf{r}, t)\right)\psi_i(\mathbf{r}, t) = i\frac{\partial\psi_i(\mathbf{r}, t)}{\partial t}. \quad (2)$$

The complexity arises in the time-dependence of the effective potential, which no longer solely depends on the electron density at time t (i.e., $\rho(\mathbf{r}, t)$). It also depends on the entire history of electron densities, the initial KS state, and the initial state of the interacting system.^{44,45}

Eq. (2) can be rearranged to provide an equation of motion for the KS one-electron reduced density matrix (1-rdm). We will indicate by \mathbf{D} the KS 1-rdm expressed in some basis set as $\rho(\mathbf{r}, t) = \sum_{\mu\nu} \mathbf{D}_{\mu\nu}(t)\chi_\mu(\mathbf{r})\chi_\nu(\mathbf{r})$ (where χ are the chosen basis functions).

The time evolution of the KS density matrix can be formulated in terms of the *Liouville-von Neumann*⁴⁶ (LvN) equation, expressed in an orthonormal basis⁴⁷ as

$$i\frac{\partial\mathbf{D}(t)}{\partial t} = \mathbf{F}(t)\mathbf{D}(t) - \mathbf{D}(t)\mathbf{F}(t), \quad (3)$$

which depends on the *time-dependent Fock matrix*, $\mathbf{F}(t)$. During the propagation, the matrix elements $\mathbf{F}(t)$ are calculated in the atomic orbital (AO) basis. In our implementation, driven by Psi4⁴⁸ and Psi4Numpy⁴⁹ frameworks, the AO basis set consists of atom-centered Gaussian-type functions, or GTOs.

The solution of the LvN equation is not straightforward for two reasons. First, in principle the dependency of $\mathbf{F}(t)$ on \mathbf{D} is very complicated and non-adiabatic. We avoid such complications by applying the adiabatic approximation and assuming that the dependency is simply given by $\mathbf{F}(t) = \mathbf{F}[\mathbf{D}(t)]$. Second, even in the adiabatic approximation, the dependency of \mathbf{F} on \mathbf{D} is highly nontrivial and includes a non-linearity that needs to be taken into account during time evolution. Thus, to handle this non-linearity, we employ a propagator approach:

$$\mathbf{D}(t) = \mathbf{U}(t, t_0)\mathbf{D}(t_0)\mathbf{U}(t, t_0)^\dagger. \quad (4)$$

Here, $\mathbf{U}(t, t_0)$ is the time evolution operator. To define the propagator, we first need to define the Fock matrix. For a non-relativistic Hamiltonian the Fock matrix, $\mathbf{F}(t)$, is expressed as

$$\mathbf{F}(t) = \mathbf{T} + \mathbf{V}_{eN} + \mathbf{V}_{xc}[\mathbf{D}(t)] + \mathbf{J}[\mathbf{D}(t)] + \mathbf{V}_{ext}(t). \quad (5)$$

Here, $\mathbf{T}_{\mu\nu} = \langle \chi_\mu | \frac{1}{2}\nabla^2 | \chi_\nu \rangle$ is the single-particle kinetic energy matrix, \mathbf{V}_{eN} is the matrix associated with the local electron-nuclear attraction potential, $v_{eN}(\mathbf{r})$. The exchange-correlation potential, $v_{xc}(\mathbf{r})$ and the classical electron-electron Coulomb repulsion, are represented by the matrices \mathbf{V}_{xc} and \mathbf{J} , respectively.

In the adiabatic approximation, the explicit time dependence in the Fock matrix arises not only from the time-dependent density, $\mathbf{D}(t)$, in the Coulomb, $\mathbf{J}[\mathbf{D}(t)]$, and exchange-correlation, $\mathbf{V}_{xc}[\mathbf{D}(t)]$, potentials but also from the contribution of the time-dependent external potential, given in matrix form as $\mathbf{V}_{ext}(t)$ (e.g., an applied laser field).

The time evolution operator is given by

$$\mathbf{U}(t, t_0) = \hat{\mathcal{T}} \exp \left(-i \int_{t_0}^t \mathbf{F}(t') dt' \right).$$

The time-ordering operator $\hat{\mathcal{T}}$ arises due to the fact that $\mathbf{F}(t)$ at different times do not necessarily commute ($[\mathbf{F}(t), \mathbf{F}(t')] \neq 0$). Sensible approximations of arbitrary precision can be made by discretizing the propagation time into short time steps. Among various propagation schemes,^{50,51} here, we adopt the second-order midpoint Magnus propagator:^{47,52,53}

$$\mathbf{U}(t + \Delta t, t) \approx \exp \left[-i \mathbf{F} \left(t + \frac{\Delta t}{2} \right) \Delta t \right].$$

2.1 Frozen density embedding in rt-TDDFT

In frozen density embedding (FDE), the electron density of the total system is partitioned into subsystem electron densities, $\{\rho_I(\mathbf{r})\}$, and is written as, $\rho_{tot}(\mathbf{r}) = \sum_{I=1}^{N_S} \rho_I(\mathbf{r})$, where N_S accounts for the total number of subsystems.

For simplicity, we consider a partition of the total density into only two contributions:

$$\rho_{tot}(\mathbf{r}) = \rho_1(\mathbf{r}) + \rho_2(\mathbf{r}). \quad (6)$$

The total electronic energy is defined as,

$$E_{tot}[\rho_1, \rho_2] = E_1[\rho_1] + E_2[\rho_2] + E_{int}[\rho_1, \rho_2],$$

where we introduce an interaction energy E_{int} which is formally bifunctional of the two subsystem densities. The subsystem energies are defined as:

$$E_I[\rho_I] = T_s[\rho_I] + E_{NN}^I + \int v_{eN}^I(\mathbf{r}) \rho_I(\mathbf{r}) d\mathbf{r} + E_H[\rho_I] + E_{xc}[\rho_I], \quad (7)$$

where $v_{eN}^I(\mathbf{r})$ denotes the electron-nuclear attraction potential of subsystem I . While $E_H[\rho_I]$ and $E_{xc}[\rho_I]$ are the Hartree and exchange-correlation energy functionals, and E_{NN}^I is the nuclear repulsion energy of subsystem I . And $T_s[\rho_I]$ is the subsystem non-interacting kinetic energy.

The interaction energy is defined as,

$$E_{int}[\rho_1, \rho_2] = T_s^{nadd}[\rho_1, \rho_2] + E_{NN}^{1,2} + \int \rho_1(\mathbf{r})v_{eN}^1(\mathbf{r})d\mathbf{r} + \int \rho_2(\mathbf{r})v_{eN}^2(\mathbf{r})d\mathbf{r} + \iint \frac{\rho_1(\mathbf{r})\rho_2(\mathbf{r}')}{|\mathbf{r} - \mathbf{r}'|}d\mathbf{r}d\mathbf{r}' + E_{xc}^{nadd}[\rho_1, \rho_2], \quad (8)$$

where the non-additive kinetic energy, $T_s^{nadd}[\rho_1, \rho_2] = T_s[\rho_{tot}] - T_s[\rho_1] - T_s[\rho_2]$, and non-additive exchange-correlation, $E_{xc}^{nadd}[\rho_1, \rho_2] = E_{xc}[\rho_{tot}] - E_{xc}[\rho_1] - E_{xc}[\rho_2]$, arise because they are not linear functionals of the density. Finally, $E_{NN}^{1,2}$ is the nuclear-nuclear repulsion of nuclei in subsystem 1 with the ones in subsystem 2.

The variational problem is given by the set of two KS equations with constrained electron density,⁵⁴ which read for subsystem 1:

$$\left(-\frac{\nabla_i^2}{2} + v_{\text{eff}}^1[\rho_1](\mathbf{r}) + v_{\text{emb}}^1[\rho_1, \rho_2](\mathbf{r}) \right) \psi_i^1(\mathbf{r}) = \epsilon_i^1 \psi_i^1(\mathbf{r}), \quad (9)$$

where $v_{\text{eff}}^1[\rho_1](\mathbf{r})$ is the subsystem 1 effective KS potential. The interaction of the electrons of subsystem 1 with the environment in FDE is represented by an embedding potential,

$$v_{\text{emb}}^1[\rho_1, \rho_2](\mathbf{r}) = v_{eN}^2(\mathbf{r}) + \int \frac{\rho_2(\mathbf{r}')}{|\mathbf{r} - \mathbf{r}'|}d\mathbf{r}' + v_{xc}^{nadd}[\rho_1, \rho_2](\mathbf{r}) + v_{T_s}^{nadd}[\rho_1, \rho_2](\mathbf{r}). \quad (10)$$

Where,

$$v_{xc}^{nadd}[\rho_1, \rho_2](\mathbf{r}) = \frac{\delta E_{xc}[\rho_{tot}]}{\delta \rho_{tot}(\mathbf{r})} - \frac{\delta E_{xc}[\rho_1]}{\delta \rho_1(\mathbf{r})}, \quad (11)$$

$$v_{T_s}^{nadd}[\rho_1, \rho_2](\mathbf{r}) = \frac{\delta T_s[\rho_{tot}]}{\delta \rho_{tot}(\mathbf{r})} - \frac{\delta T_s[\rho_1]}{\delta \rho_1(\mathbf{r})}. \quad (12)$$

Due to the direct dependence of the non-additive terms on both subsystem densities, ρ_{tot} , an approximation for the exchange-correlation and kinetic energy functionals and potentials must be employed. Pure density functionals are used, providing a clear and simple way to evaluate all non-additive terms. Similar to the exchange-correlation functional approximants, there are several options for the kinetic energy, such as the Thomas-Fermi⁵⁵ kinetic energy functional, or other GGA-based functionals.^{56,57}

The set of coupled equations, Eq. (9) and Eq. (10), can be solved iteratively using a Freeze-and-Thaw⁵⁸ procedure, which is repeated until all the subsystems' densities converge. Once the embedding potential is obtained, $v_{emb}^1[\rho_1, \rho_2](\mathbf{r})$, it is added to the usual Fock Hamiltonian, by computing its matrix elements in the atomic orbitals basis. The μ, ν element is

$$(\mathbf{V}_{emb}^1)_{\mu\nu} = \int \chi_\mu(\mathbf{r}) v_{emb}^1[\rho_1, \rho_2](\mathbf{r}) \chi_\nu(\mathbf{r}) d\mathbf{r}. \quad (13)$$

The uncoupled real-time FDE TDDFT scheme (*uFDE-rt-TDDFT*), in which ρ_2 is kept frozen and therefore does not respond to the external perturbation, is implemented³⁹ by adding the matrix representation of the embedding potential, Eq. (13), to the time-dependent Fock matrix, Eq. (5), for the “active” subsystem 1, which reads as,

$$\mathbf{F}^1(t) = \mathbf{T}^1 + \mathbf{V}_{nuc}^1 + \mathbf{V}_{xc}[\rho_1(t)] + \mathbf{J}[\rho_1(t)] + \mathbf{V}_{ext}(t) + \mathbf{V}_{emb}[\rho_1(t), \rho_2], \quad (14)$$

where we have included explicitly the functional dependence of each term.

Clearly, a time dependence is added to the embedding potential, which needs to be updated during the propagation, even though the density of the environment, ρ_2 , is taken

to be frozen.

2.2 Block-Orthogonalized Manby-Miller embedding in rt-TDDFT

Block-Orthogonalized Manby-Miller embedding (BOMME)^{59,60} is a mean-field embedding approach that partitions the total system into two different domains, A and B, treated with two different levels of theory. In this method, a high-level Fock matrix is assigned to the domain requiring accurate treatment (usually A), while the remaining part of the system (domain B) is described by a low-level Fock matrix. To accomplish this, instead of using the conventional atomic-orbital (AO) basis, the high and low levels of theory are encoded by a block-orthogonal (BO) basis. Thus, a basis set transformation matrix \mathbf{O} is formulated,

$$\mathbf{O} = \begin{pmatrix} \mathbf{I}^{AA} & -\mathbf{P}^{AB} \\ \mathbf{0} & \mathbf{I}^{BB} \end{pmatrix}. \quad (15)$$

This matrix explores the projection of the non-orthogonal AO basis set into the BO basis set. Here the diagonal terms, \mathbf{I}^{AA} and \mathbf{I}^{BB} , account for the identity matrices of domains A and B, respectively, with dimensions corresponding to the sizes of their respective basis sets (n_a and n_b). While, $\mathbf{P}^{AB} = (\mathbf{S}^{AA})^{-1}\mathbf{S}^{AB}$ corresponds to the projection matrix, where \mathbf{S}^{AB} is the AO overlap between the atomic orbitals assigned to domains A and B.

By considering AA(BB) block to denote the domain approached with a high-(low-) level of theory, the *time-dependent* Fock matrix in the BO basis reads as,

$$\mathbf{F}(t) = \tilde{\mathbf{h}}_0 + \tilde{\mathbf{G}}^{Low}[\tilde{\mathbf{D}}(t)] + (\tilde{\mathbf{G}}^{High}[\tilde{\mathbf{D}}^{AA}(t)] - \tilde{\mathbf{G}}^{Low}[\tilde{\mathbf{D}}^{AA}(t)]) + \mathbf{V}_{ext}(t), \quad (16)$$

where $\tilde{\mathbf{h}}_0$ correspond to the one-electron operator, while $\mathbf{G}[\tilde{\mathbf{D}}(t)]$ denoted the two-electron

terms in the BO basis. The foregoing is obtained by the following transformations,

$$\tilde{\mathbf{h}}_0 = \mathbf{O}^T \mathbf{h}_0 \mathbf{O} \quad (17)$$

$$\tilde{\mathbf{G}}[\tilde{\mathbf{D}}(t)]^{High/Low} = \mathbf{O}^T \mathbf{G}[\mathbf{D}(t)]^{High/Low} \mathbf{O} \quad (18)$$

$$\tilde{\mathbf{D}}(t) = \mathbf{O}^T \mathbf{D}(t) \mathbf{O}, \quad (19)$$

where \mathbf{h}_0 and $\mathbf{G}[\mathbf{D}(t)]$ corresponds to the one and two electrons terms in the AO basis,

$$\mathbf{h}_0 = \mathbf{T} + \mathbf{V}_{eN} \quad (20)$$

$$\mathbf{G}[\mathbf{D}(t)] = \mathbf{J}[\mathbf{D}(t)] + c_x \mathbf{K}[\mathbf{D}(t)] + c_x \mathbf{V}_{xc}[\mathbf{D}(t)], \quad (21)$$

and c_x is the fraction of the exact Hartree-Fock exchange in the exchange-correlation potential \mathbf{V}_{xc} . The exchange term in $\mathbf{G}[\mathbf{D}(t)]^{High}$ is calculated by considering only the exact exchange interaction within the AA block.⁴³ This method is called *BOMME-rt-TDDFT*.

2.3 Multilevel embedding in rt-TDDFT

Up to now, we have described two types of embedding methods. One, FDE, splits a system into two or more subsystems which are then allowed to interact via orbital-free non-additive functionals. The second method, BOMME, splits a system into domains at the density matrix level, using a basis set representation. BOMME then treats one domain (called A) with one DFT method (called *High*), and the other domain (called B) with another DFT method (called *Low*). In this work, we combine the two approaches in a single method called multilevel embedding rt-TDDFT or ML-rt-TDDFT. This integration ensures that strongly interacting fragments in a system are treated with BOMME, while weakly interacting fragments are managed with FDE. By doing so, we leverage the excellent behavior of BOMME for reproducing density and energy of strongly-interacting fragments^{27,39} and that of FDE for reproducing density and energy of weakly-interacting fragments.^{61,62} ML-rt-TDDFT com-

pletely avoids a KS-DFT calculation of the full system affording massive computational savings. In practice, ML-rt-TDDFT prescribes the solution of Kohn-Sham-like equations in which an FDE embedding potential is added to the BOMME Fock matrix, both with and without the external perturbation. With that, the time-dependent Fock matrix in Eq. (16) reads

$$\mathbf{F}(t) = \tilde{\mathbf{h}}_0 + \tilde{\mathbf{G}}^{Low}[\tilde{\mathbf{D}}(t)] + (\tilde{\mathbf{G}}^{High}[\tilde{\mathbf{D}}^{AA}(t)] - \tilde{\mathbf{G}}^{Low}[\tilde{\mathbf{D}}^{AA}(t)]) + \mathbf{V}_{ext}(t) + \mathbf{V}_{emb}^1[\rho_1(t), \rho_2].$$

With such a definition, one introduces an intermediate layer (the low-level BOMME region, or domain B) between domain A (e.g. a solute, in our case the halide ions) and the FDE environment. This reduces computational cost in treating the entirety of subsystem 1 with the high-level of theory. While, in principle, one could employ FDE to treat domains A and B as two additional subsystems, the use of BOMME instead allows for a more reliable treatment of stronger interactions within the domains, since the use of approximate non-additive kinetic energy density functionals (NAKEs), which are unable to capture strong interactions^{63,64} is avoided. It also alleviates the storage burden associated with employing a common basis set for the whole system. Considering the long propagation times necessary to simulate core spectra, reducing computational complexity and storage requirements is particularly welcome.

It should be noted that in the prior *uFDE-rt-TDDFT* implementation³⁹ (see text after Eq. (13)), due to implementation issues, the computational time required to evaluate the embedding potential $v_{emb}[\rho^1(t), \rho_2](\mathbf{r})$ in Eq. (10), in the uncoupled scheme at each time iteration was found to increase linearly with the number of water molecules surrounding the solute. This increase poses a challenge, with the computation of Eq. (13) being the most time-consuming step. This required the use of a step-wise updating strategy for calculating the embedding potential matrix $\mathbf{V}_{emb}[\rho_1(t), \rho_2]$, which showed promising performance when updated every 30 steps throughout the simulation time. However, this approach can become

problematic due to variations in the density of the active system, seriously compromising its use in further production calculations.

To address the efficiency issue in evaluating the embedding potential, Eq. (10), we have explored the reimplementations of two crucial PyBertha functions (namely *embpot2mat.py* and *denstogrid.py* from the *psi4embprt.py* module) (Referred as “partial” GPU-aware implementation) employing two optimize tensor libraries, PyTorch⁶⁵ and TensorFlow,⁶⁶ in view of their ability to offload matrix operations to GPUs while remaining very similar to the Numpy API (thus requiring rather localized changes to the Numpy-based prior implementation). We have also reimplemented all Numpy matrix operations (Referred as “full” GPU-aware implementation) of the *util.py* function of the *psi4rt* module along with the aforementioned PyBertha functions. This was done because the *mo_fock_mid_forwd_eval.py* of *util.py* continuously evaluates the Hartree-Fock, Exchange, and Coulomb matrices by adding the analytical δ -function pulse at each iteration along the real-time propagation. Further implementation details are available in the supplementary material (Section ??).

The results of the total timing for a single snapshot (SN-14 of chloride embedded in its first solvation shell) using both “full” and “partial” implementations are displayed in figures A and B of Fig. 1, respectively. By using PyTorch and TensorFlow, we reduced simulation time from 48 to 16 and 26 hours, respectively when the partial GPU implementation is used. Interestingly, the embedding potential calculations (referred to as the “*Vemb calculation*”) are three times faster with TensorFlow than with the conventional CPU implementation, and almost twice as fast with PyTorch when partial implementation is used, Figure B in Fig. 1. Surprisingly, when we include the full optimization, Figure A in Fig. 1, including *psi4rt.py* functions, the TensorFlow time increases while the PyTorch time decreases, thus in the “Partial” TensorFlow the embedding potential evaluation (“*Vemb calculation*”) differs by 10 hours with respect to partial PyTorch implementation.

The above can be rationalized by looking at basic profiling results for the module *psi4embprt.py* for both “partial” and “full” GPU implementations, Fig. 2. These profiling results

indicate that 49.5% of the total time is spent in the *embpot2mat.py* module when a CPU-only (Numpy-based) implementation is used, left-hand side figure in Fig. 2. In the TensorFlow and PyTorch partial implementations, the time spent on the same routine, *embpot2mat.py*, decreases to 1.6% and 29.0%, respectively. This is not the case when the “full” implementation is profiled where the time spent in the *embpot2mat.py* is reduced to 16.0% in the PyTorch case and 1.8% in the TensorFlow case. We attribute these differences to the continuous transfer of data between Numpy arrays on the CPU and TensorFlow tensors on the GPU, which is known to negatively affect the performance of TensorFlow.⁶⁷ This is especially true when transitioning from partial to full implementation, as the latter involves more matrix-tensor transformations. Despite this, we insist on the main point of employing optimized tensor libraries, which is to provide significant performance improvements with relatively minor changes to the Numpy-based code. In subsequent optimizations of the code work, we plan to better characterize this point, while attempting to eliminate other performance bottlenecks.

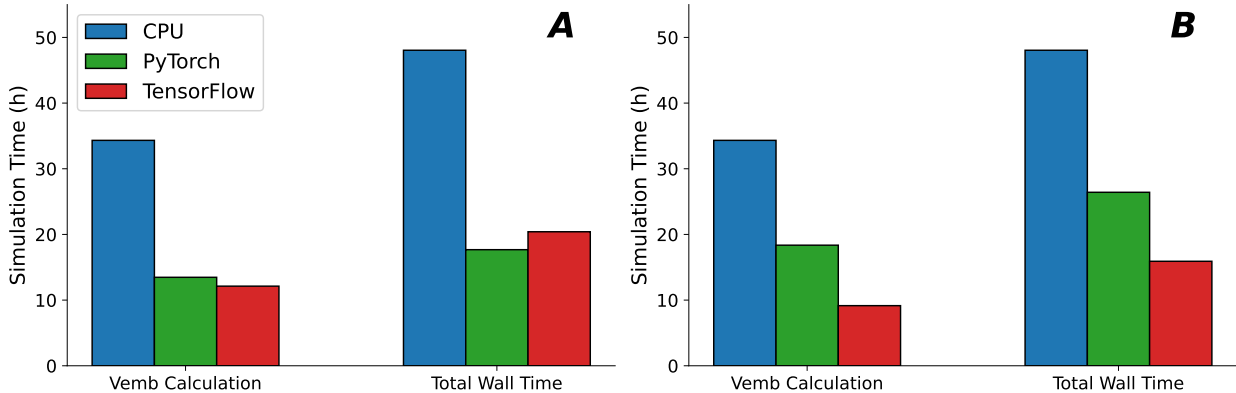


Figure 1: Time profile of GPU implementation. Insight A: Full implementation in *psi4rt.py* module along with the aforementioned PyBertha functions (Full GPU implementation). Insight B: Total time in seconds spent by the main Python functions (*embpot2mat.py* and *denstogrid.py*) involved in the evaluation of Eq. 10 in *psi4embprt.py* module of PyBertha code (Partial GPU implementation). The time corresponds to the total time spent in the function per call. The total number of calls of both functions is 29 007. The percentages are obtained by cProfile and Snakeviz⁶⁸ packages. The total simulation time is 33.9 fs, for a total of 56 000 steps, with a length of 0.025 a.u. per time step.

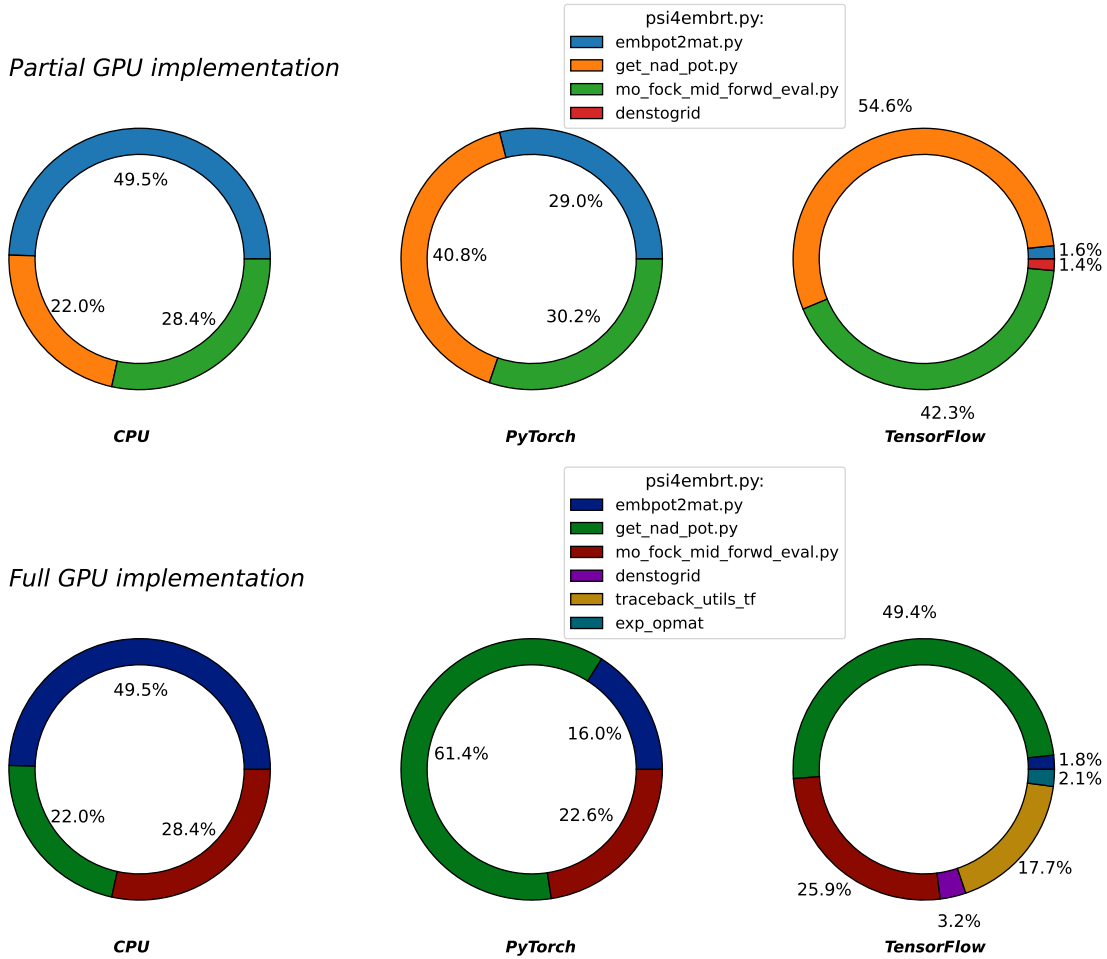


Figure 2: Profiling results for the main Python functions (*embpot2mat.py* and *denstogrid.py*) involved in the evaluation of Eq. 10 in *psi4embprt.py* module of PyBertha code (Partial GPU implementation). And the full implementation in *psi4rt.py* module along with the aforementioned PyBertha functions (Full GPU implementation). The percentages are obtained by cProfile and Snakeviz⁶⁸ packages. An interactive version of the Profile can be found in the Zenodo repository 10.5281/zenodo.10570083.

Computational details

ML-rt-TDDF real-time framework, was implemented as part of PyBertha^{69–71} package in the *numercialtest* branch of PyBertha version 64f6752.⁷² PyBertha is a code based on Psi4Numpy⁴⁹ framework, here we used Psi4⁷³ version 1.8a1.dev5. *BOMME-rt-TDDFT* real-time code, also coupled to the PyBertha package is available in the GitHub repository (version ba72aec⁷⁴). Examples of user usage are published in the Zenodo repository 10.5281/zenodo.10570083.

We modified the previously published version³⁹ of *uFDE-rt-TDDFT* in PyBertha repository, by re-implementing the projection of the $(\mathbf{V}_{\text{emb}}^i)_{\mu\nu}$ into the AO basis, see Eq. 13 with PyTorch 1.13.1⁶⁵ (code available in the Git-Hub revision c3e1a57⁷⁵) and TensorFlow 2.13.0⁶⁶ (code available in the Git-Hub revision 88092d1⁷⁶).

In *uFDE-rt-TDDFT* approach, we employed two schemes, where halides served as active subsystems (subsystem 1), and were embedded in 1) 8 water molecules; and 2) 50 water molecules, as subsystem 2. For subsystem 1, we employed the B3LYP functional⁷⁷ with an aug-cc-pVTZ⁷⁸ basis set. The embedding potential of the active subsystem for the remaining water molecules was calculated employing BLYP functional and a DZP basis set.⁷⁹ The benchmarking was carried out using 4 OpenMP threads and 1 GPU NVIDIA A100-PCIE-40GB device. We also investigated the effect of the relaxation of the density of the environment, by implementing the Freeze and thaw (FaT) procedure of PyADF⁸⁰ into *uFDE-rt-TDDFT* and *ML-rt-TDDF* codes. Thus, one can start the time-propagation with environment ground-state densities which are either “relaxed” (from a prior FaT calculation with 5 cycles) or “unrelaxed”.

In *ML-rt-TDDFT*, the halides (domain A) and their first solvation shell (8 water molecules) (domain B) made up the active subsystem or subsystem 1, while the remaining water molecules (up to 50) belonged to the environment subsystem, subsystem 2. For the active subsystem, the halide was calculated at B3LYP, while for the surrounding waters up to 8 molecules, we used BLYP as exchange-correlation functional, with the aug-cc-pVDZ⁷⁸ and

DZP basis sets, respectively. To include the embedding potential $(\mathbf{V}_{\text{emb}}^i)_{\mu\nu}$ of the remaining 42 waters in *ML-rt-TDDF*, we used ADF⁸¹ version 2019.403, employing the PyADF⁸⁰ code. Environment subsystem calculations were carried out with a DZP⁸² Slater Type Orbitals basis set that differs from the one used by the Psi4 package (Gaussian Type Orbitals) at the BLYP level. The setup for the active subsystem or subsystem 1, in *ML-rt-TDDFT* described above is employed in *BOMME-rt-TDDFT* calculations, with the halide being Domain A (B3LYP/aug-cc-pVDZ), and first solvation shell Domain B (BLYP/DZP) but with a Gaussian Type Orbital base package.

In all the real-time simulations, the initial electron density δ_0 is perturbed by an analytical δ -function pulse with a strength of $\kappa = 5.0 \times 10^{-5}$ a.u. along x, y, and z directions. The induced dipole moment was kept in each iteration for a total of 56 000 steps, with a length of 0.025 a.u. per time step. Thus, the total simulation time is 33.9 fs for both halides. Similarly, as previous works,^{39,41} we employed a Padé approximant-based Fourier Transform (FFT)⁸³ with an exponential damping $e^{-\lambda t}$ with $\lambda = 3.0 \cdot 10^{-4}$ a.u..

All real-time simulations were carried out utilizing 10 configurations for both the fluoride and chloride systems. These were selected from snapshots of 10 ns-long classical molecular dynamics trajectories of halides in water carried out by Réal et al.⁶ and cut out to build 50 water droplets as used in the study by Bouchafra et al.³⁶ (see Fig. 3). Out of these structure, we selected five snapshots based on the water binding energies (BE) predicted by employing the relativistic equation-of-motion coupled-cluster and FDE.³⁶ Specifically, we considered the geometries with the closest BEs concerning the average binding energy of the $1b_1$ peak. Similarly, we choose the other five geometries based on the closest representative geometries concerning the binding energy distribution of the corresponding halide.

We utilized an ensemble approach⁸⁴ which involved averaging over multiple core excitations obtained from 10 snapshots per system. In the ensemble approach, the excitation peaks obtained after the Fourier transform (FFT) were convoluted with a Gaussian function of width $\sigma=0.7$ eV, which was centered at each excitation. The final step involved summing

the convoluted peaks to create the absorption spectrum.

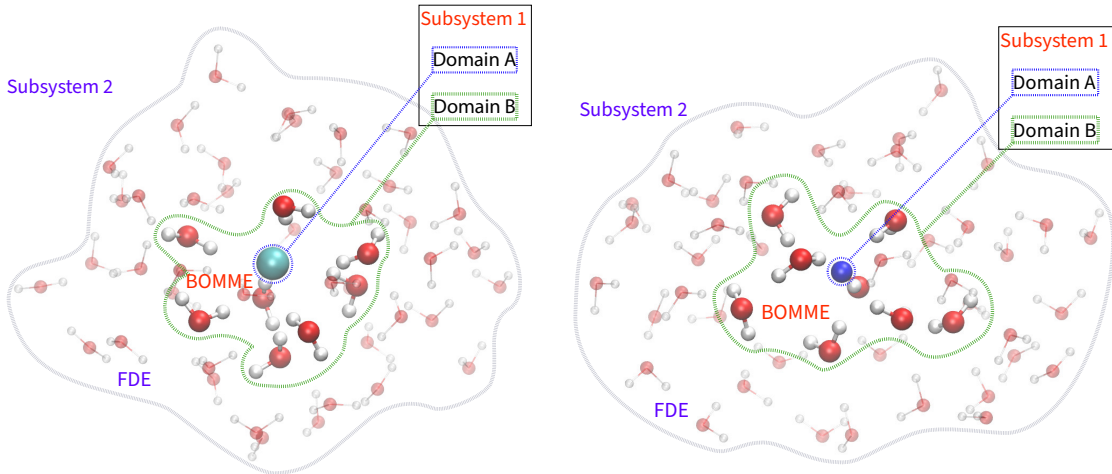


Figure 3: Schematic representation of the multilevel approach for embedding chloride (Right) and fluoride (Left) anions in up to 50 water molecules. Subsystem 1 corresponds to the set of Domain A: Halides (Cl^- , and F^-) and Domain B: water first solvation shell (up to 8 water molecules). Subsystem 2 corresponds to the second or outer shell (up to 50 water molecules)

3 Results and discussion

3.1 $[\text{X}(\text{H}_2\text{O})_8]^-$ models

Before discussing the performance of *ML-rt-TDDFT* calculations on the $[\text{X}(\text{H}_2\text{O})_{50}]^-$ models and its comparison to experiment, it is instructive to explore the behavior of uncoupled FDE and BOMME for the smaller $[\text{X}(\text{H}_2\text{O})_8]^-$ models (Subsystem 1). Some of us have previously carried out⁴¹ a similar comparison for the K-edges of chloride and fluoride, and the L_1 -edge of chloride. In this context, the same general conclusions persist regarding the relative merits and shortcomings of FDE and BOMME. However, the prior calculations only explored a single structure, whereas here, we extend the analysis to consider the effect of configurational averaging on the calculated spectra. This discussion is crucial as it will later contribute to the exploration of the impact of outer solvation shells on the spectra. Additionally, we systematically investigate the effect of the relaxation of the ground-

state density of the environment (after several FaT cycles) in FDE calculations in a more systematic manner than in previous work.

3.1.1 uFDE rt-TDDFT

The *uFDE-rt-TDDFT* simulated XAS spectrum for chloride, using “unrelaxed” and “relaxed” ground-state densities $\rho_0(\mathbf{r})$ is shown in Fig. 4. Starting with the K-edge, the first feature peak over 2762 eV relates to the electronic transition from the 1s core state to (n+1)p valence state of the chloride anion. Similarly, the second peak can be assigned to the 1s \rightarrow (n+2)p transition.⁴¹ We observe a solvatochromic blue shift of 0.69 eV for the first and 0.16 eV for the second absorption peak, respectively, for the “relaxed” calculations with respect to the “unrelaxed” ones. This underscores the higher sensitivity of the orbitals in the valence region (including the lower-lying (n+1)p virtuals) to the relaxation of the density,³⁶ this is expected since we are dealing with a charged species that will strongly polarize the first solvation shell.

By inspecting insets A and B for the first K-edge peak in Fig. 4, non-negligible differences in intensity and peak positions among different snapshots are noticeable. These are consequences of the asymmetrical first solvation shell,³⁶ which affects more strongly the lower-lying virtual molecular orbitals of the halide.⁷ Therefore, upon taking into account the configurational averaging, we end up with peaks that are broader than those obtained from the individual structures. An opposite behavior is observed in the case of the second peak, which shows no significant changes in intensities and a negligible displacement in peak positions among different snapshots, see Fig. ?? in the supplementary material.

The *uFDE-rt-TDDFT* results for the L₁-edge, also shown in Fig. 4, corresponds to the electronic transition from the 2s electronic state of chloride anion to (n+1)p. In contrast to the K-edge, there seems to be no significant effect from both the relaxation of the ground-state density and configurational averaging. Thus, the transition to (n+1)p virtual electronic states presents a “sharp” line-like absorption.⁸⁵

For the K-edge spectrum of fluoride, shown in Fig. 4, the *uFDE-rt-TDDFT* paint, in qualitative terms, a very similar picture as for chloride. However, due to the interaction between fluoride and water being significantly stronger than that of chloride (evident from the radial distribution function between fluoride anion and water-oxygen,⁶ which peaks at a distance of 2.6 Å, whereas for the average distance between chloride and water-oxygen is almost twice as much at 3.4 Å²), we see a larger blue shift (1.09 eV) for the first peak, and a slightly smaller one (0.13 eV) for the second peak when the ground-state electron density is relaxed (after several FaT cycles). This picture is consistent with the heightened impact of relaxation on valence and low-lying virtual orbitals, and with the suggestion that fluoride forms the most stable hydrate species.²

Despite the broadening introduced by configurational averaging, the agreement between the *uFDE-rt-TDDFT* chloride K-edge spectra and experiment remains relatively poor. The first feature is not broad enough, which we can attribute to the inability of *uFDE-rt-TDDFT* to reproduce a second peak at 2765 eV, which has been found to arise from the coupling between chloride and the near-neighbor waters.⁴¹ In addition to that, while the second peak in the 2772–2775 eV region is present, it is not as broad as in the experiment.

Determining the K-edge XAS spectra of solvated fluoride anion remains a challenge for soft X-ray absorption spectroscopy.⁸⁶ Therefore, direct comparison between our simulated ensemble spectra and experimental data is not possible. Nevertheless, it is instructive to observe the differences and similarities between chloride and fluoride.

3.1.2 BOMME rt-TDDFT

In the top panel of Fig. 5 we present *BOMME-rt-TDDFT* results for the chloride and fluoride XAS spectra. Starting with the chloride K-edge XAS spectra, we see that in contrast to *uFDE-rt-TDDFT*, we have one intense additional peak in the region between 2764–2768 eV, a less intense one between 2770 eV and 2772 eV, and a third feature near 2780 eV. We observe that configurational averaging brings about important changes in the spectrum, not

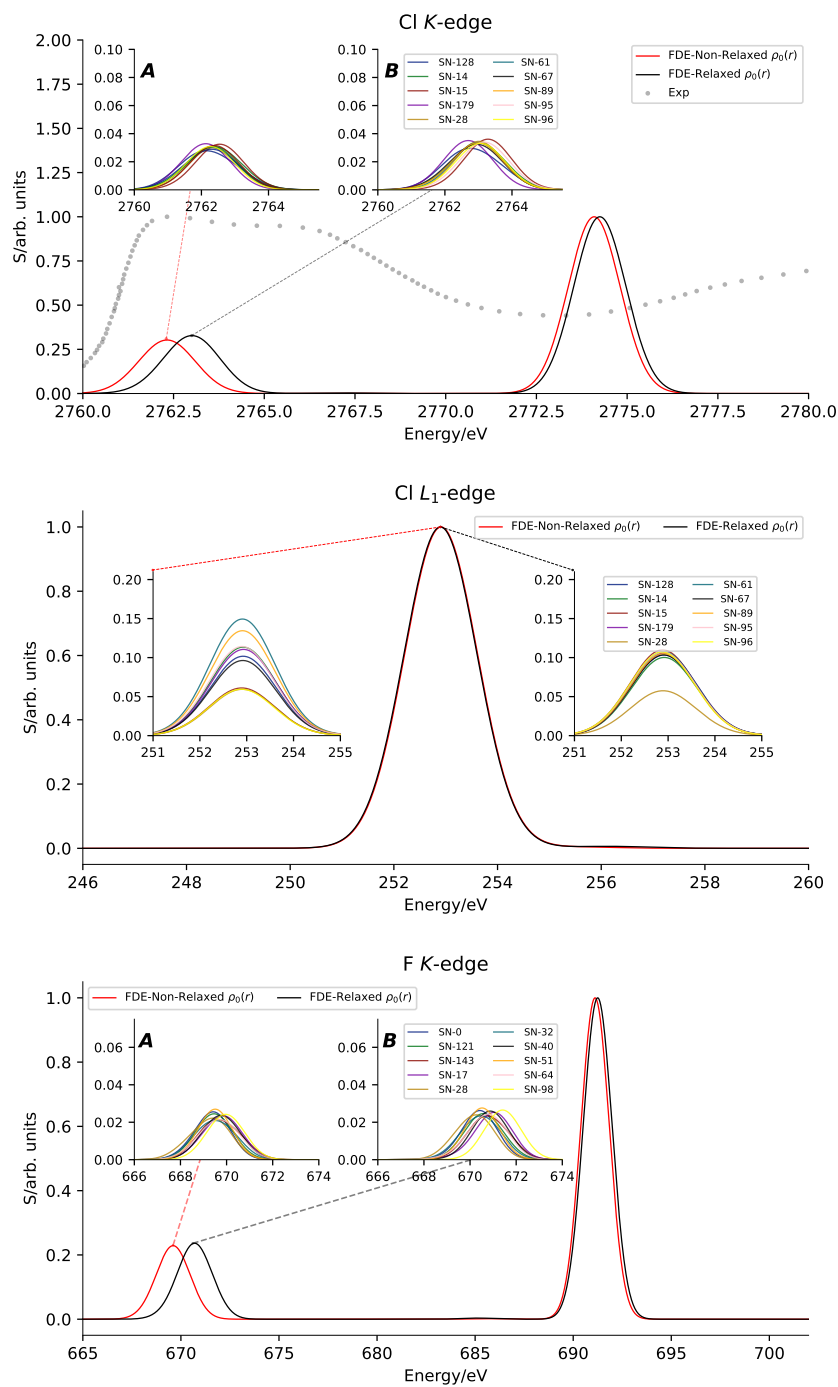


Figure 4: Chloride K-edge (top) and L₁-edge (middle) as well as fluoride K-edge (bottom) X-ray absorption spectra for the anions embedded in their first solvation shell (8 water molecules) between the energy range of the free ion edge peak and up to 20 eV (Cl K-edge), 14 eV (Cl L₁-edge), and 35 eV (F K-edge). Data was obtained by employing *FDE-rt-TDDFT* with a non-relax and relaxed initial density $\rho(r)$. 5 cycles of Freeze and Thaw were employed to obtain a relaxed initial density. Inset pictures show the contribution per snapshot. A Gaussian broadening ($\sigma = 0.7$ eV) was used.

only in terms of the broadening of the peaks, but also in terms of intensities, and that different structures contribute differently to different parts of the spectrum; for instance, SN-15 exhibits the highest intensity compared to all other snapshots around the second and third peaks. We examined the radial distribution function (See Fig. ?? in the supplementary information) between chloride and the closest water molecules and observed that the water molecules furthest away from the chloride are closer to it in comparison to other snapshots, explaining the slightly higher intensities.

For the chloride L_1 -edge, as shown in the middle panel of Fig. 5, we now observe three peaks: the most intense one in the 254–256 eV range (as in the *uFDE-rt-TDDFT* results), a significantly less intense peak in the 248–252 eV range, and another intense peak in the 258–260 eV range. While the first two peaks were reported before,⁴¹ the use of configurational averaging not only broadens the less intense peak but also makes it gain in intensity. For the most intense peaks, similar to the K-edge, some configurations contribute more than others to the spectrum, while contributions are more homogeneous for the first peak.

In the fluoride K-edge spectrum, as seen in the bottom panel of Fig. 5, we also observe additional features in the 675–688 eV region with respect to *uFDE-rt-TDDFT* results, with an overall redshift relative to the latter. However, these are not as intense as the features in the 668–675 eV and 690–700 eV regions. A marked difference between fluoride and chloride lies in the contributions from different configurations to the spectrum.

While, as discussed above for chloride, different configurations contribute differently to different regions of the spectrum, for fluoride contributions around 695 eV are significantly more important than those for lower energies. In contrast, for chloride, the contributions are by and large similar across the whole energy range under consideration. This results in a much more intense peak at around 695 eV than in the near-edge region.

The additional peaks observed in comparison to *uFDE-rt-TDDFT* were previously attributed to the coupling of the response between chloride and the first solvation shell.⁴¹ In this analysis, we have further examined the transition density (TD) of a couple of excited

states, employing the B3LYP functional for the whole system– there is a small difference compared to the BOMME calculations, which combine B3LYP for chlorine and BLYP for the water molecules.

The TD analysis indicates (see Fig. ?? in the supplementary information) that the first two peaks (within the 2760–2768 eV window) predominantly arise from $1s \rightarrow (n+1)p$ transitions, whereas states in the 2775–2780 eV correspond to the $1s \rightarrow (n+2)p$ transitions, as indicated by their larger spatial extent.

The TD for the chloride L_1 -edge (figure ?? in the supplementary information) and fluoride K-edge paint a similar picture as for the chloride K-edge, with transitions being predominantly centered on the halide. For fluoride (Fig. ?? in the supplementary information), we note distorted $1s$ character on the halide in the range of intermediate peaks (680–685 eV), while in the final and most prominent peak (695 eV), we noticed even higher distortions of the halide orbitals, likely caused by the presence of surrounding water molecules.

That said, while the TDs does not show very marked charge-transfer excitations from chloride or fluoride to the water ligands, the comparison between *BOMME-rt-TDDFT* (which allows for contributions from the waters in the excited state) and *uFDE-rt-TDDFT* (which does not) leaves no question as to the importance of going beyond a model in which only the halide belongs to the active subsystem.

Considering now comparison with the experiment for the chloride K-edge, we can observe that the spectral feature in the near-edge (2760–2766 eV) is semi-quantitatively recovered in the *BOMME rt-TDDFT* calculations, with significant differences coming from depletion of intensity around 2763 eV, and a more pronounced decrease in intensity at around 2766 eV in the *BOMME rt-TDDFT* calculations. Furthermore, for energies above 2775 eV, the *BOMME rt-TDDFT* intensities are significantly larger than in the experiment. These represent in any case a significant improvement over the FDE results.

Interestingly, in comparison to the supermolecular result (for a single snapshot, see supplementary information, Fig. ??), we see (a) a better qualitative agreement between *BOMME*

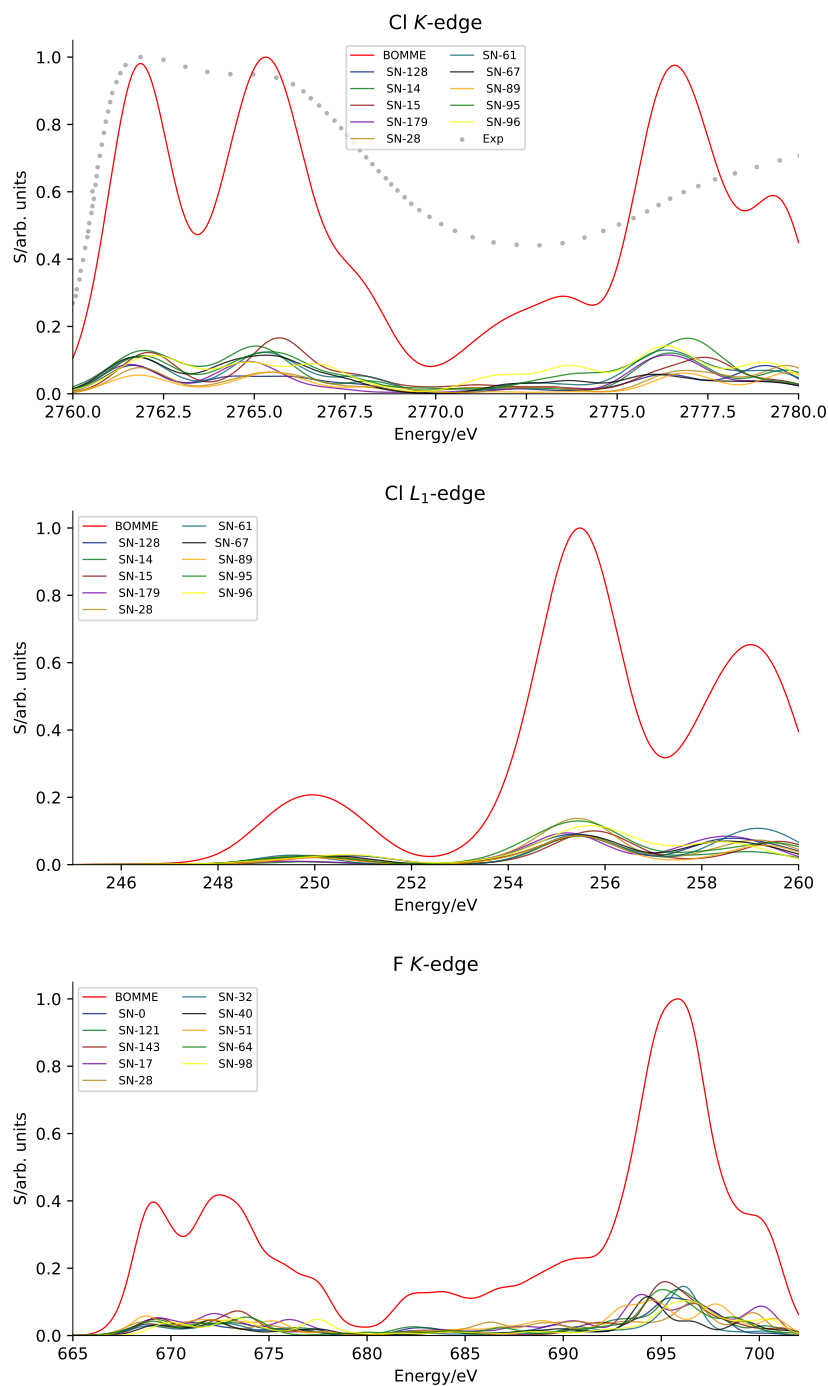


Figure 5: Chloride K-edge (top) and L₁-edge (middle) and fluoride K-edge (bottom) X-ray absorption spectra for the anions embedded in their first solvation shell (8 water molecules) between the energy range of the free ion edge peak and up to 20 eV (Cl K-edge), 14 eV (Cl L₁-edge), and 35 eV (F K-edge). Data was obtained by employing *BOMME-rt-TDDFT*. Inset pictures show the contribution per snapshot. A Gaussian broadening ($\sigma = 0.7$ eV) was used.

rt-TDDFT and experiment for the near-edge feature (below 2770 eV), since the supermolecular calculations show an intense peak at about 2763 eV, with lower-intensity features at 2762 eV and 2767.5 eV, respectively. On the other hand, supermolecule calculations show less intense features around 2775–2780 eV. Given our findings from the effect of configurational averaging, we can expect supermolecule calculations to show an overall increase in intensity, but without significant changes in the overall shape of the spectrum.

3.2 $[\text{X}(\text{H}_2\text{O})_{50}]^-$ models

Before discussing the *ML-rt-TDDFT* results, we note that we have not carried out *BOMME rt-TDDFT* calculations for the $[\text{X}(\text{H}_2\text{O})_{50}]^-$ models since the computational cost of such simulations over the different snapshots was beyond the computational means at our disposal. We have on the other hand carried out *uFDE-rt-TDDFT* calculations for these larger systems, with only the halides making up the active subsystem, subsystem 1 and subsystem 2 being the 50-water droplet. However, since we have observed no noticeable difference between these calculations and those discussed above, we do not discuss these further, and the corresponding spectra are shown in Fig. ??, ??, and ?? in the supplementary information.

3.2.1 Multilevel embedding *rt-TDDFT*

It has been shown that the chloride anion significantly changes the structure of water beyond the first solvation shell even outside its second solvation shell.⁸⁷ Thus, in *ML-rt-TDDF* we take into account not only the immediate response of the first solvation shell on the anion, subsystem 1, as discussed in the *BOMME rt-TDDFT* section, but also the extended response of the second and outermost solvation shells, subsystem 2, up to 50 water molecules.

The results for the chloride K-edge XAS spectra are shown in the top Fig. 6. Comparing the spectra obtained by *BOMME rt-TDDFT* with those obtained by *ML-rt-TDDF*, see supplementary information Fig. ??, reveals that in the latter the intensity of features at around 2766 eV and 2776 eV are reduced, while the feature near-edge (2762.5 eV) remains

intense, besides the blue shift of 2.94 eV. With respect to the effect of configurational averaging for the feature at around 2766 eV, we see that contributions from the different snapshots are more similar to each other. We note that from the TD analysis for one snapshot (SN=128, see Fig. ?? in the supplementary information), the picture of a mostly chloride-centered, 1s to (n+1)p transition remains for the features below 2770 eV.

With the introduction of a FDE embedding potential in *ML-rt-TDDF*, it becomes of interest to investigate the effect of the relaxation of the ground-state density (after several FaT cycles) for the second solvation shell and beyond has on the spectrum—one would, in any case, expect that this effect to be smaller than for the first solvation shell, since the exact response of the first solvation shell would, by and large, be accounted for by the *BOMME* treatment of the halide subsystem. We confirm this to be the case, with rather small shifts being observed between the ‘relaxed’ and ‘unrelaxed’ models. However, we note small non-negligible intensities differences between the two models for the features at 2766 eV and 2776 eV, see top Fig. 6.

The comparison between *BOMME rt-TDDFT* and *ML-rt-TDDF* chloride L₁-edge XAS spectrum shows that the latter results in a blue shift of 0.38 eV, see supplementary information Fig. ?. The peak with the highest intensity is located at 255.84 eV for *ML-rt-TDDF*. Much like for the K-edge, there are only rather small differences between ‘relaxed’ and ‘unrelaxed’ models.

The difference between *BOMME rt-TDDFT* and *ML-rt-TDDF* for the K-Edge spectrum of fluoride, on the other hand, is remarkable with an energy blue shift of 1.9 eV of *ML-rt-TDDF* with respect to *BOMME rt-TDDFT*, see supplementary information Fig. ?. We observe in Fig. 6 that in *ML-rt-TDDF*, the near-edge peaks are now the most intense ones, with several features within energies above 680 eV with much smaller intensities. While in Fig. 5, *BOMME rt-TDDFT* presents the high-intensity feature at 695 eV, this feature shows the most significant difference between *BOMME rt-TDDFT* and *ML-rt-TDDF*. In addition to that, the difference between the ‘relaxed’ and ‘unrelaxed’ models in *ML-rt-TDDF* is

significant for the feature at around 675 eV, while for the rest of the spectrum, differences are minor.

Based on our analysis, we can conclude that the intensities of the second feature of the near-edge peak are influenced by the relaxation of the outer shell, subsystem 2, in the simulation of the K-edge for both Cl^- and F^- systems. However, the first feature remains unchanged due to its origin from the explicit response of the first solvation shell over the halide, which is treated with *BOMME*. It is this response that will be affected the most by the K-edge signal upon density relaxation. Thus, by including a long-range effect through the embedding potential (Eq. 10), the intensity of the second feature of the near-edge peak decreases around 0.2 arb. units. The overall spectra are in agreement with the spectra obtained using the real-time TDDFT module of NwChem, see supplementary information Fig. ??.

We have successfully addressed two significant challenges that were previously encountered in predicting XAS: (1) the need for a substantial set of solvent configurations to generate accurate XAS spectra. (2) the accuracy of the theory used: particularly the exchange-correlation functional. We have overcome both obstacles by sampling snapshots from a 50 ns simulation³⁶ and by using hybrid exchange-correlation functionals to describe the activated subsystem 1 in our *BOMME* and *ML - rtTDDFT* approaches.⁸⁸

4 Conclusions

In this work, we have presented a novel quantum embedding approach in which projection-based (BOMME) and density-based (FDE) methods are combined. The resulting approach seems particularly well-suited to tackle systems in which some subsystems interact strongly (e.g. a solute and its first solvation shell) while others interact more weakly (a solute and its second solvation shell) while maintaining a relatively low computational cost.

We have applied this approach to investigate the X-ray absorption spectra of chloride and

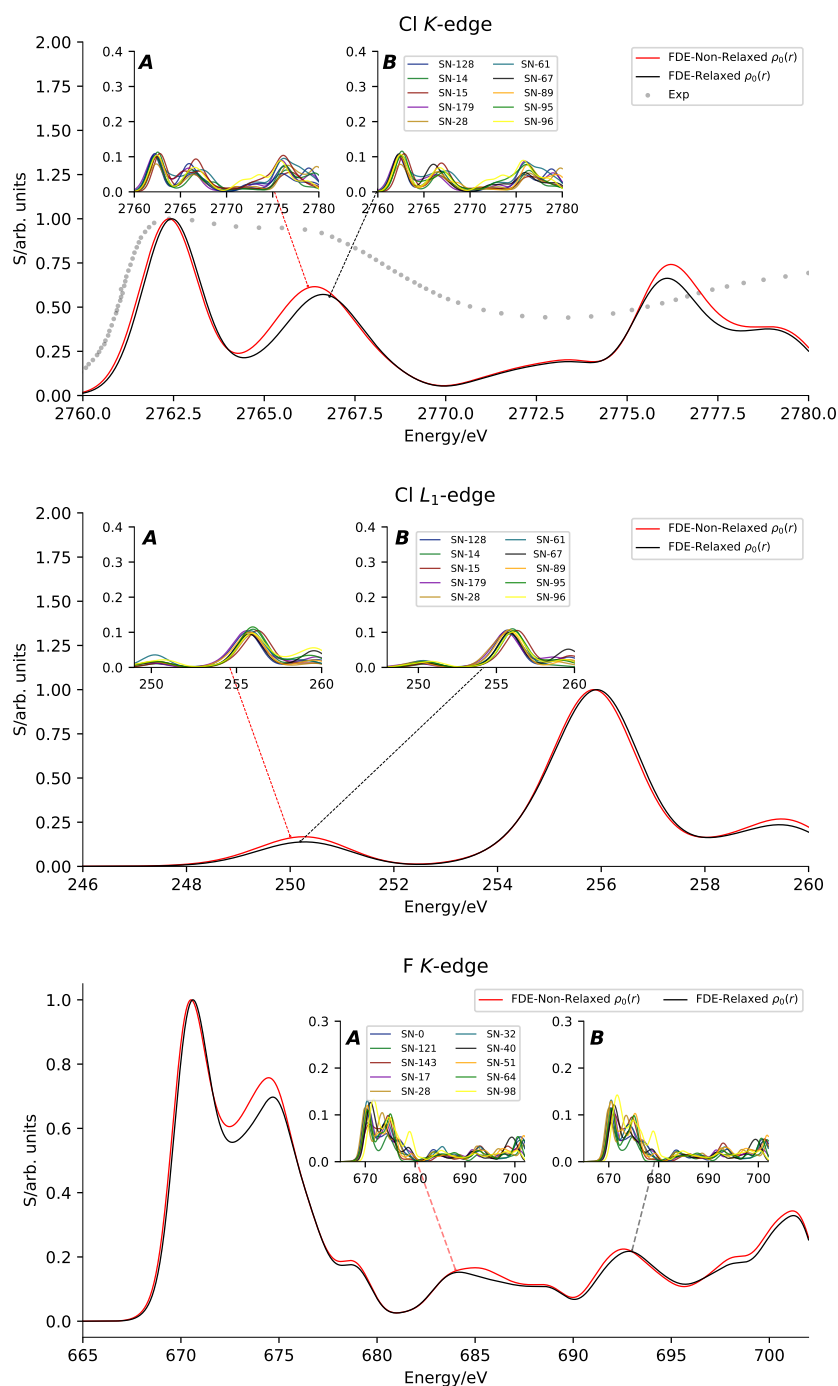


Figure 6: Chloride K-Edge (top) and L_1 -Edge (middle) and fluoride K-Edge (bottom) X-ray absorption spectra for the anions embedded in their first solvation shell (8 water molecules) between the energy range of the free ion edge peak and up to 20 eV (Cl K-edge), 14 eV (Cl L_1 -edge), and 25 eV (F K-edge). Data was obtained by employing *ML-rt-TDDFT* with a non-relax and relaxed initial density $\rho(r)$. 5 cycles of Freeze and Thaw were employed to obtain a relaxed initial density. Inset pictures show the contribution per snapshot. A Gaussian broadening ($\sigma = 0.7$ eV) was used.

fluoride in aqueous solutions (based on a 50-water droplet model) through real-time time-dependent DFT calculations in order to investigate how core spectra at the K and L₁ edges are changed by employing configurational averaging (by considering several snapshots from classical molecular dynamics simulations with polarizable force fields). Furthermore, we have explored the use of optimized tensor libraries (PyTorch and TensorFlow) to eliminate some of the performance bottlenecks of our prior implementations of real-time TDDFT quantum embedding.

We have found that configuration averaging is important not only as a means of broadening the different features of the spectra but also can have profound effects on the intensities— and in this respect, we have shown that contributions to the final intensities for a particular energy range generally arise from different structures.

We have also observed that the near-edge features, which predominantly involve the lowest-lying virtual orbitals centered on the halides, are somewhat more sensitive to the quality of the embedding models. This is especially in the case of FDE, for which the representation of charged systems requires the relaxation (several FaT cycles) of ground-state electron density of the first solvation shell, but less so for the other approaches (BOMME) since this relaxation is implicitly taken into account with the optimization of the orbitals for the halide plus first solvation sphere subsystem 1.

Contrary to valence and core ionization energies, for chloride we have found that embedding models in which the halide-water interactions are approximated (e.g. by having only the halide in active subsystem region, subsystem 1, in the case of FDE) are not capable of reproducing the experimental spectrum. At the same time, we observed that spectra with the BOMME approach tend to overestimate intensities, especially for features in higher energies. By taking into account the second solvation shell through FDE, this effect is counteracted, resulting in an overall better agreement with the experiment across the energy window considered here.

Finally, given the difficulties associated with the analysis of transitions in real-time

TDDFT simulations, for selected structures, we carried out an analysis of transition density for these systems, and from those established that the transitions for the edges under consideration can be considered as dominated by transitions within the halide system. The comparison between embedding approaches shows that, albeit small, the interactions between the halides are nevertheless essential to obtain agreement with experiment results.

Acknowledgement

MDS, VV, and ASPG acknowledge funding from projects CPER WaveTech, Labex CaPPA (Grant No. ANR-11-LABX-0005-01), CompRIXS (Grant Nos. ANR-19CE29-0019 and DFG JA 2329/6-1), the I-SITE ULNE project OVERSEE and MESONM International Associated Laboratory (LAI) (Grant No. ANR-16-IDEX-0004), as well support from the French regional (Mésocentre de l'Université de Lille) and national supercomputing facilities (Grant Nos. DARI A0110801859 and A0130801859). JAMB acknowledges support from the Chateaubriand Fellowship of the Office for Science & Technology of the Embassy of France in the United States. MP acknowledges support from the National Science Foundation under grants No. CHE-2154760 and OAC-2117429.

Supporting Information Available

The data (input/output) corresponding to the calculations of this paper are available at the Zenodo repository under DOI: 10.5281/zenodo.10570083.

The Supporting Information is available free of charge on the ACS Publications website at DOI: XXX. [add description of what is in the SI].

References

- (1) Muralidharan, A.; Pratt, L.; Chaudhari, M.; Rempe, S. Quasi-chemical theory for anion hydration and specific ion effects: Cl^- (aq) vs. F^- (aq). *Chem. Phys. Lett.* **2019**, *737*, 100037, DOI: 10.1016/j.cpletx.2019.100037.
- (2) Hofer, T. S. Solvation Structure and Ion-Solvent Hydrogen Bonding of Hydrated Fluoride, Chloride and Bromide—A Comparative QM/MM MD Simulation Study. *Liquids* **2022**, *2*, 445–464, DOI: 10.3390/liquids2040026.
- (3) Chowdhuri, S.; Chandra, A. Dynamics of Halide Ion-Water Hydrogen Bonds in Aqueous Solutions: Dependence on Ion Size and Temperature. *J. Phys. Chem. B* **2006**, *110*, 9674–9680, DOI: 10.1021/jp057544d.
- (4) Heuft, J. M.; Meijer, E. J. Density functional theory based molecular-dynamics study of aqueous fluoride solvation. *J. Chem. Phys.* **2005**, *122*, 094501, DOI: 10.1063/1.1853352.
- (5) Bakker, H. J. Structural Dynamics of Aqueous Salt Solutions. *Chem. Rev.* **2008**, *108*, 1456–1473, DOI: 10.1021/cr0206622.
- (6) Réal, F.; Severo Pereira Gomes, A.; Guerrero Martínez, Y. O.; Ayed, T.; Galland, N.; Masella, M.; Vallet, V. Structural, dynamical, and transport properties of the hydrated halides: How do At^- bulk properties compare with those of the other halides, from F^- to I^- ? *J. Chem. Phys.* **2016**, *144*, 124513, DOI: 10.1063/1.4944613.
- (7) Antalek, M.; Pace, E.; Hedman, B.; Hodgson, K. O.; Chillemi, G.; Benfatto, M.; Sarangi, R.; Frank, P. Solvation structure of the halides from x-ray absorption spectroscopy. *J. Chem. Phys.* **2016**, *145*, 044318, DOI: 10.1063/1.4959589.
- (8) Marin, T. W.; Janik, I.; Bartels, D. M.; Chipman, D. M. Failure of molecular dynamics to provide appropriate structures for quantum mechanical description of the aqueous

- chloride ion charge-transfer-to-solvent ultraviolet spectrum. *Phys. Chem. Chem. Phys.* **2021**, *23*, 9109–9120, DOI: 10.1039/D1CP00930C.
- (9) Waluyo, I.; Nordlund, D.; Bergmann, U.; Schlesinger, D.; Pettersson, L. G. M.; Nilsson, A. A different view of structure-making and structure-breaking in alkali halide aqueous solutions through x-ray absorption spectroscopy. *J. Chem. Phys.* **2014**, *140*, 244506, DOI: 10.1063/1.4881600.
- (10) Collins, K. D. The behavior of ions in water is controlled by their water affinity. *Q. Rev. Biophys.* **2019**, *52*, e11, DOI: 10.1017/S0033583519000106.
- (11) Fang, Z.; Li, M.; Wang, L.; Duan, X.; Zhao, H. A long-life aqueous Fluoride-ion battery based on Water-in-salt electrolyte. *Inorg. Chem. Commun.* **2023**, *148*, 110275, DOI: 10.1016/j.inoche.2022.110275.
- (12) Mao, Y.; Zhou, T.; Xu, L.; Wu, W.; Wang, R.; Xiong, Z.; Wu, D.; Shi, H. Molecular understanding of aqueous electrolyte properties and dielectric effect in a CDI system. *Chem. Eng. J.* **2022**, *435*, 134750, DOI: 10.1016/j.cej.2022.134750.
- (13) Kulik, H. J.; Marzari, N.; Correa, A. A.; Prendergast, D.; Schwegler, E.; Galli, G. Local Effects in the X-ray Absorption Spectrum of Salt Water. *J. Phys. Chem. B* **2010**, *114*, 9594–9601, DOI: 10.1021/jp103526y.
- (14) Alayoglu, P.; Chang, T.; Yan, C.; Chen, Y.; Mankad, N. P. Uncovering a CF_3 Effect on X-ray Absorption Energies of $[\text{Cu}(\text{CF}_3)_4]^-$ and Related Copper Compounds by Using Resonant Diffraction Anomalous Fine Structure (DAFS) Measurements**. *Angew. Chem.* **2023**, e202313744, DOI: 10.1002/ange.202313744.
- (15) Zhang, Y.; Xie, R.; Long, T.; Günzing, D.; Wende, H.; Ollefs, K. J.; Zhang, H. Autonomous atomic Hamiltonian construction and active sampling of X-ray absorption spectroscopy by adversarial Bayesian optimization. *npj Comput. Mater.* **2023**, *9*, 46, DOI: 10.1038/s41524-023-00994-w.

- (16) Zhao, W.; Chu, W.; Yang, F.; Yu, M.; Chen, D.; Guo, X.; Zhou, D.; Shi, N.; Marcelli, A.; Niu, L.; Teng, M.; Gong, W.; Benfatto, M.; Wu, Z. Quantitative investigation of two metallohydrolases by X-ray absorption spectroscopy near-edge spectroscopy. *Nucl. Instrum. Methods Phys. Res., Sect. A* **2007**, *580*, 451–456, DOI: 10.1016/j.nima.2007.05.196.
- (17) Tofoni, A.; Tavani, F.; Persson, I.; D’Angelo, P. P K-Edge XANES Calculations of Mineral Standards: Exploring the Potential of Theoretical Methods in the Analysis of Phosphorus Speciation. *Inorg. Chem.* **2023**, *62*, 11188–11198, DOI: 10.1021/acs.inorgchem.3c01346.
- (18) Herbert, J. M.; Zhu, Y.; Alam, B.; Ojha, A. K. Time-Dependent Density Functional Theory for X-ray Absorption Spectra: Comparing the Real-Time Approach to Linear Response. *J. Chem. Theory Comput.* **2023**, *19*, 6745–6760, DOI: 10.1021/acs.jctc.3c00673.
- (19) Misael, W. A.; Severo Pereira Gomes, A. Core Excitations of Uranyl in $\text{Cs}_2\text{UO}_2\text{Cl}_4$ from Relativistic Embedded Damped Response Time-Dependent Density Functional Theory Calculations. *Inorg. Chem.* **2023**, *62*, 11589–11601, DOI: 10.1021/acs.inorgchem.3c01302.
- (20) Park, W.; Komarov, K.; Lee, S.; Choi, C. H. Mixed-Reference Spin-Flip Time-Dependent Density Functional Theory: Multireference Advantages with the Practicality of Linear Response Theory. *J. Phys. Chem. Lett.* **2023**, *14*, 8896–8908, DOI: 10.1021/acs.jpcllett.3c02296.
- (21) Fransson, T.; Pettersson, L. G. M. Calibrating TDDFT Calculations of the X-ray Emission Spectrum of Liquid Water: The Effects of Hartree–Fock Exchange. *J. Chem. Theory Comput.* **2023**, *19*, 7333–7342, DOI: 10.1021/acs.jctc.3c00728.
- (22) Liekhus-Schmaltz, C. E.; Ho, P. J.; Weakly, R. B.; Aquila, A.; Schoenlein, R. W.;

- Khalil, M.; Govind, N. Ultrafast x-ray pump x-ray probe transient absorption spectroscopy: A computational study and proposed experiment probing core-valence electronic correlations in solvated complexes. *J. Chem. Phys.* **2021**, *154*, 214107, DOI: 10.1063/5.0047381.
- (23) Pezeshki, S.; Lin, H. Molecular dynamics simulations of ion solvation by flexible-boundary QM/MM: On-the-fly partial charge transfer between QM and MM subsystems. *J. Comput. Chem.* **2014**, *35*, 1778–1788, DOI: 10.1002/jcc.23685.
- (24) Gomez, D. T.; Pratt, L. R.; Asthagiri, D. N.; Rempe, S. B. Hydrated Anions: From Clusters to Bulk Solution with Quasi-Chemical Theory. *Acc. Chem. Res.* **2022**, *55*, 2201–2212, DOI: 10.1021/acs.accounts.2c00078.
- (25) Andreussi, O.; Fisicaro, G. Continuum embeddings in condensed-matter simulations. *Int. J. Quantum Chem.* **2019**, *119*, e25725, DOI: 10.1002/qua.25725.
- (26) Milanese, J. M.; Provorse, M. R.; Alameda, E.; Isborn, C. M. Convergence of Computed Aqueous Absorption Spectra with Explicit Quantum Mechanical Solvent. *J. Chem. Theory Comput.* **2017**, *13*, 2159–2171, DOI: 10.1021/acs.jctc.7b00159.
- (27) Ding, F.; Manby, F. R.; Miller, T. F. Embedded Mean-Field Theory with Block-Orthogonalized Partitioning. *J. Chem. Theory Comput.* **2017**, *13*, 1605–1615, DOI: 10.1021/acs.jctc.6b01065.
- (28) Sharma, M.; Sierka, M. Efficient Implementation of Density Functional Theory Based Embedding for Molecular and Periodic Systems Using Gaussian Basis Functions. *J. Chem. Theory Comput.* **2022**, *18*, 6892–6904, DOI: 10.1021/acs.jctc.2c00380.
- (29) Wesolowski, T. A.; Shedge, S.; Zhou, X. Frozen-Density Embedding Strategy for Multilevel Simulations of Electronic Structure. *Chem. Rev.* **2015**, *115*, 5891–5928, DOI: 10.1021/cr500502v.

- (30) Iannuzzi, M.; Kirchner, B.; Hutter, J. Density functional embedding for molecular systems. *Chem. Phys. Lett.* **2006**, *421*, 16–20, DOI: 10.1016/j.cplett.2005.08.155.
- (31) Krishtal, A.; Ceresoli, D.; Pavanello, M. Subsystem real-time time dependent density functional theory. *J. Chem. Phys.* **2015**, *142*, 154116, DOI: 10.1063/1.4918276.
- (32) Jacob, C. R.; Neugebauer, J. Subsystem density-functional theory: Subsystem density-functional theory. *Wiley Interdiscip. Rev.: Comput. Mol. Sci.* **2014**, *4*, 325–362, DOI: 10.1002/wcms.1175.
- (33) Fu, M.; Wesolowski, T. A. Excitation Energies of Embedded Chromophores from Frozen-Density Embedding Theory Using State-Specific Electron Densities of the Environment. *J. Phys. Chem. A* **2023**, *127*, 535–545, DOI: 10.1021/acs.jpca.2c07747.
- (34) Niemeyer, N.; Eschenbach, P.; Bensberg, M.; Tölle, J.; Hellmann, L.; Lampe, L.; Mas-solle, A.; Rikus, A.; Schnieders, D.; Unsleber, J. P.; Neugebauer, J. The subsystem quantum chemistry program SERENITY. *WIREs Comput. Mol. Sci.* **2023**, *13*, e1647, DOI: 10.1002/wcms.1647.
- (35) Sen, S.; Visscher, L. Towards the description of charge transfer states in solu-bilised LHCII using subsystem DFT. *Photosynth. Res.* **2023**, *156*, 39–57, DOI: 10.1007/s11120-022-00950-7.
- (36) Bouchafra, Y.; Shee, A.; Réal, F.; Vallet, V.; Severo Pereira Gomes, A. Predictive Simulations of Ionization Energies of Solvated Halide Ions with Relativistic Embedded Equation of Motion Coupled Cluster Theory. *Phys. Rev. Lett.* **2018**, *121*, 266001, DOI: 10.1103/PhysRevLett.121.266001.
- (37) Opoku, R. A.; Toubin, C.; Gomes, A. S. P. Simulating core electron binding energies of halogenated species adsorbed on ice surfaces and in solution *via* relativistic quan-tum embedding calculations. *Phys. Chem. Chem. Phys.* **2022**, *24*, 14390–14407, DOI: 10.1039/D1CP05836C.

- (38) Höfener, S.; Gomes, A. S. P.; Visscher, L. Solvatochromic shifts from coupled-cluster theory embedded in density functional theory. *J. Chem. Phys.* **2013**, *139*, 104106, DOI: 10.1063/1.4820488.
- (39) De Santis, M.; Belpassi, L.; Jacob, C. R.; Severo Pereira Gomes, A.; Tarantelli, F.; Visscher, L.; Storchi, L. Environmental Effects with Frozen-Density Embedding in Real-Time Time-Dependent Density Functional Theory Using Localized Basis Functions. *J. Chem. Theory Comput.* **2020**, *16*, 5695–5711, DOI: 10.1021/acs.jctc.0c00603.
- (40) De Santis, M.; Sorbelli, D.; Vallet, V.; Gomes, A. S. P.; Storchi, L.; Belpassi, L. Frozen-Density Embedding for Including Environmental Effects in the Dirac-Kohn–Sham Theory: An Implementation Based on Density Fitting and Prototyping Techniques. *J. Chem. Theory Comput.* **2022**, *18*, 5992–6009, DOI: 10.1021/acs.jctc.2c00499.
- (41) De Santis, M.; Vallet, V.; Gomes, A. S. P. Environment Effects on X-Ray Absorption Spectra With Quantum Embedded Real-Time Time-Dependent Density Functional Theory Approaches. *Front. Chem.* **2022**, *10*, 823246, DOI: 10.3389/fchem.2022.823246.
- (42) Koh, K. J. Development of RT-TDDFT for the Interaction With the Explicit Solvent and for Correct Description of Excitation Process - ProQuest. 2020; <https://www.proquest.com/docview/2624742534?pq-origsite=gscholar&fromopenview=true>, Graduate Program in Chemistry and Biochemistry.
- (43) Koh, K. J.; Nguyen-Beck, T. S.; Parkhill, J. Accelerating Realtime TDDFT with Block-Orthogonalized Manby–Miller Embedding Theory. *J. Chem. Theory Comput.* **2017**, *13*, 4173–4178, DOI: 10.1021/acs.jctc.7b00494.
- (44) Vignale, G. Real-time resolution of the causality paradox of time-dependent density-functional theory. *Phys. Rev. A* **2008**, *77*, 062511, DOI: 10.1103/PhysRevA.77.062511.

- (45) Maitra, N. T. Perspective: Fundamental aspects of time-dependent density functional theory. *J. Chem. Phys.* **2016**, *144*, 220901, DOI: 10.1063/1.4953039.
- (46) Jakowski, J.; Morokuma, K. Liouville–von Neumann molecular dynamics. *J. Chem. Phys.* **2009**, *130*, 224106, DOI: 10.1063/1.3152120.
- (47) Li, X.; Smith, S. M.; Markevitch, A. N.; Romanov, D. A.; Levis, R. J.; Schlegel, H. B. A time-dependent Hartree–Fock approach for studying the electronic optical response of molecules in intense fields. *Phys. Chem. Chem. Phys.* **2005**, *7*, 233–239, DOI: 10.1039/B415849K.
- (48) Turney, J. M.; Simmonett, A. C.; Parrish, R. M.; Hohenstein, E. G.; Evangelista, F. A.; Fermann, J. T.; Mintz, B. J.; Burns, L. A.; Wilke, J. J.; Abrams, M. L.; Russ, N. J.; Leininger, M. L.; Janssen, C. L.; Seidl, E. T.; Allen, W. D.; Schaefer, H. F.; King, R. A.; Valeev, E. F.; Sherrill, C. D.; Crawford, T. D. Psi4: an open-source *ab initio* electronic structure program: Psi4: an electronic structure program. *Wiley Interdiscip. Rev.: Comput. Mol. Sci.* **2012**, *2*, 556–565, DOI: 10.1002/wcms.93.
- (49) Smith, D. G. A.; Burns, L. A.; Sirianni, D. A.; Nascimento, D. R.; Kumar, A.; James, A. M.; Schriber, J. B.; Zhang, T.; Zhang, B.; Abbott, A. S.; Berquist, E. J.; Lechner, M. H.; Cunha, L. A.; Heide, A. G.; Waldrop, J. M.; Takeshita, T. Y.; Ale-naizan, A.; Neuhauser, D.; King, R. A.; Simmonett, A. C.; Turney, J. M.; Schaefer, H. F.; Evangelista, F. A.; DePrince, A. E.; Crawford, T. D.; Patkowski, K.; Sherrill, C. D. Psi4NumPy: An Interactive Quantum Chemistry Programming Environment for Reference Implementations and Rapid Development. *J. Chem. Theory Comput.* **2018**, *14*, 3504–3511, DOI: 10.1021/acs.jctc.8b00286.
- (50) Press, W. H.; Teukolsky, S. A. *Numerical Recipes 3rd Edition: The Art of Scientific Computing*; Cambridge University Press, 2007; Google-Books-ID: 1aA0dzK3FegC.
- (51) Meng, S.; Kaxiras, E. Real-time, local basis-set implementation of time-dependent den-

- sity functional theory for excited state dynamics simulations. *J. Chem. Phys.* **2008**, *129*, 054110, DOI: 10.1063/1.2960628.
- (52) Magnus, W. On the exponential solution of differential equations for a linear operator. *Commun. Pure Appl. Math.* **1954**, *7*, 649–673, DOI: 10.1002/cpa.3160070404.
- (53) Casas, F.; Iserles, A. Explicit Magnus expansions for nonlinear equations. *J. Phys. A: Math. Gen.* **2006**, *39*, 5445–5461, DOI: 10.1088/0305-4470/39/19/S07.
- (54) Wesolowski, T.; Warshel, A. Ab initio free energy perturbation calculations of solvation free energy using the frozen density functional approach. *J. Phys. Chem.* **1994**, *98*, 5183–5187, DOI: <https://doi.org/10.1021/j100071a003>.
- (55) Thomas, L. H. The calculation of atomic fields. *Mathematical Proceedings of the Cambridge Philosophical Society* **1927**, *23*, 542–548, DOI: 10.1017/S0305004100011683.
- (56) Laricchia, S.; Fabiano, E.; Constantin, L.; Della Sala, F. Generalized gradient approximations of the noninteracting kinetic energy from the semiclassical atom theory: Rationalization of the accuracy of the frozen density embedding theory for nonbonded interactions. *J. Chem. Theory Comput.* **2011**, *7*, 2439–2451, DOI: <https://doi.org/10.1021/ct200382w>.
- (57) Lembarki, A.; Chermette, H. Obtaining a gradient-corrected kinetic-energy functional from the Perdew-Wang exchange functional. *Phys. Rev. A* **1994**, *50*, 5328–5331, DOI: 10.1103/PhysRevA.50.5328.
- (58) Wesolowski, T. A.; Weber, J. Kohn-Sham equations with constrained electron density: an iterative evaluation of the ground-state electron density of interacting molecules. *Chem. Phys. Lett.* **1996**, *248*, 71–76, DOI: [https://doi.org/10.1016/0009-2614\(95\)01281-8](https://doi.org/10.1016/0009-2614(95)01281-8).

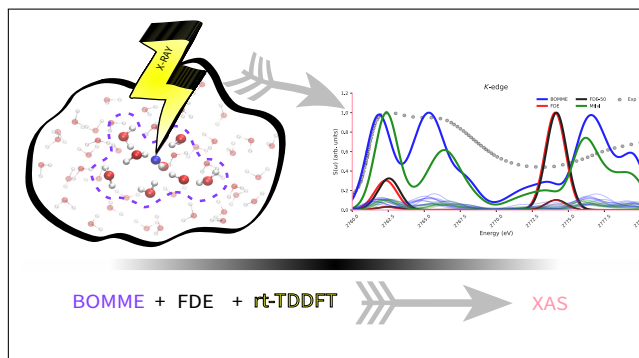
- (59) Manby, F. R.; Stella, M.; Goodpaster, J. D.; Miller, T. F. A Simple, Exact Density Functional-Theory Embedding Scheme. *J. Chem. Theory Comput.* **2012**, *8*, 2564–2568, DOI: 10.1021/ct300544e.
- (60) Pipolo, S.; Corni, S.; Cammi, R. The cavity electromagnetic field within the polarizable continuum model of solvation. *J. Chem. Phys.* **2014**, *140*, 164114, DOI: 10.1063/1.4871373.
- (61) Gomes, A. S. P.; Jacob, C. R.; Visscher, L. Calculation of local excitations in large systems by embedding wave-function theory in density-functional theory. *Phys. Chem. Chem. Phys.* **2008**, *10*, 5353, DOI: 10.1039/b805739g.
- (62) Höfener, S.; Severo Pereira Gomes, A.; Visscher, L. Molecular properties via a subsystem density functional theory formulation: A common framework for electronic embedding. *J. Chem. Phys.* **2012**, *136*, DOI: 10.1063/1.3675845.
- (63) Konecny, L.; Kadek, M.; Komorovsky, S.; Malkina, O. L.; Ruud, K.; Repisky, M. Acceleration of Relativistic Electron Dynamics by Means of X2C Transformation: Application to the Calculation of Nonlinear Optical Properties. *J. Chem. Theory Comput.* **2016**, *12*, 5823–5833, DOI: 10.1021/acs.jctc.6b00740.
- (64) Repisky, M.; Konecny, L.; Kadek, M.; Komorovsky, S.; Malkin, O. L.; Malkin, V. G.; Ruud, K. Excitation Energies from Real-Time Propagation of the Four-Component Dirac–Kohn–Sham Equation. *J. Chem. Theory Comput.* **2015**, *11*, 980–991, DOI: 10.1021/ct501078d.
- (65) Imambi, S.; Prakash, K. B.; Kanagachidambaresan, G. R. In *Programming with TensorFlow: Solution for Edge Computing Applications*; Prakash, K. B., Kanagachidambaresan, G. R., Eds.; EAI/Springer Innovations in Communication and Computing; Springer International Publishing: Cham, 2021; pp 87–104, DOI: 10.1007/978-3-030-57077-4_10.

- (66) TensorFlow Developers, TensorFlow. 2021; <https://zenodo.org/record/4758419>.
- (67) Michelucci, U. *Advanced Applied Deep Learning*; Apress: Berkeley, CA, 2019; pp 27–77, DOI: 10.1007/978-1-4842-4976-5_2.
- (68) Davis, M., et al. SnakeViz, an in-browser Python profile viewer. 2021.
- (69) Storchi, L.; De Santis, M.; Belpassi, L. In *Advances in Parallel Computing*; Foster, I., Joubert, G. R., Kučera, L., Nagel, W. E., Peters, F., Eds.; IOS Press, 2020; DOI: 10.3233/APC200060.
- (70) De Santis, M.; Storchi, L.; Belpassi, L.; Quiney, H. M.; Tarantelli, F. PyBERTHART: A Relativistic Real Time Four Component TDDFT Implementation Using Prototyping Techniques Based on Python. *J. Chem. Theory Comput.* **2020**, *16*, 2410–2429, DOI: 10.1021/acs.jctc.0c00053.
- (71) Belpassi, L.; De Santis, M.; Quiney, H. M.; Tarantelli, F.; Storchi, L. BERTHA: Implementation of a four-component Dirac–Kohn–Sham relativistic framework. *J. Chem. Phys.* **2020**, *152*, 164118, DOI: 10.1063/5.0002831.
- (72) De Santis, M.; Martinez, J.; Vallet, V.; Gomes, A. S. P.; Sorbelli, D.; Storchi, L.; Belpassi, L.; Jacob, C. R.; Tarantelli, F. BOMME-RT. <https://github.com/RelMBdev/pybertha/tree/numericaltest>, 2013.
- (73) Smith, D. G. A.; Burns, L. A.; Simmonett, A. C.; Parrish, R. M.; Schieber, M. C.; Galvelis, R.; Kraus, P.; Kruse, H.; Di Remigio, R.; Alenaizan, A.; James, A. M.; Lehtola, S.; Misiewicz, J. P.; Scheurer, M.; Shaw, R. A.; Schriber, J. B.; Xie, Y.; Glick, Z. L.; Sirianni, D. A.; O’Brien, J. S.; Waldrop, J. M.; Kumar, A.; Hohenstein, E. G.; Pritchard, B. P.; Brooks, B. R.; Schaefer, H. F.; Sokolov, A. Y.; Patkowski, K.; DePrince, A. E.; Bozkaya, U.; King, R. A.; Evangelista, F. A.; Turney, J. M.; Crawford, T. D.; Sherrill, C. D. Psi4 1.4: Open source software

- for high throughput quantum chemistry. *J. Chem. Phys.* **2020**, *152*, 184108, DOI: 10.1063/5.0006002.
- (74) De Santis, M.; Martinez, J.; Vallet, V.; Gomes, A. S. P.; Sorbelli, D.; Storchi, L.; Belpassi, L.; Jacob, C. R.; Tarantelli, F. BOMME-RT. https://github.com/RelMBdev/bomme_rt/tree/fock_helper_restart, 2013.
- (75) De Santis, M.; Martinez, J.; Vallet, V.; Gomes, A. S. P.; Sorbelli, D.; Storchi, L.; Belpassi, L.; Jacob, C. R.; Tarantelli, F. Pybertha-Psi4emdr. https://github.com/RelMBdev/pybertha/tree/psi4rt-pytorch-mixed_basis, 2023.
- (76) De Santis, M.; Martinez, J.; Vallet, V.; Gomes, A. S. P.; Sorbelli, D.; Storchi, L.; Belpassi, L.; Jacob, C. R.; Tarantelli, F. Pybertha-Psi4emdr. https://github.com/RelMBdev/pybertha/tree/psi4rt-tensorflow-mixed_basis, 2023.
- (77) Becke, A. D. Density-functional thermochemistry. III. The role of exact exchange. *J. Chem. Phys.* **1993**, *98*, 5648–5652, DOI: 10.1063/1.464913.
- (78) Papajak, E.; Zheng, J.; Xu, X.; Leverentz, H. R.; Truhlar, D. G. Perspectives on Basis Sets Beautiful: Seasonal Plantings of Diffuse Basis Functions. *J. Chem. Theory Comput.* **2011**, *7*, 3027–3034, DOI: 10.1021/ct200106a.
- (79) Dunning, T. H. Gaussian Basis Functions for Use in Molecular Calculations. I. Contraction of (9s5p) Atomic Basis Sets for the First-Row Atoms. *J. Chem. Phys.* **1970**, *53*, 2823–2833, DOI: 10.1063/1.1674408.
- (80) Jacob, C. R.; Beyhan, S. M.; Bulo, R. E.; Gomes, A. S. P.; Götz, A. W.; Kiewisch, K.; Sikkema, J.; Visscher, L. PyADF - A scripting framework for multiscale quantum chemistry. *J. Comput. Chem.* **2011**, *32*, 2328–2338, DOI: 10.1002/jcc.21810.
- (81) Te Velde, G.; Bickelhaupt, F. M.; Baerends, E. J.; Fonseca Guerra, C.; Van Gisber-

- gen, S. J. A.; Snijders, J. G.; Ziegler, T. Chemistry with ADF. *J. Comput. Chem.* **2001**, *22*, 931–967, DOI: 10.1002/jcc.1056.
- (82) Van Lenthe, E.; Baerends, E. J. Optimized Slater-type basis sets for the elements 1–118. *J. Comput. Chem.* **2003**, *24*, 1142–1156, DOI: 10.1002/jcc.10255.
- (83) Bruner, A.; LaMaster, D.; Lopata, K. Accelerated Broadband Spectra Using Transition Dipole Decomposition and Padé Approximants. *J. Chem. Theory Comput.* **2016**, *12*, 3741–3750, DOI: 10.1021/acs.jctc.6b00511.
- (84) Zuehlsdorff, T. J.; Isborn, C. M. Modeling absorption spectra of molecules in solution. *Int. J. Quantum Chem.* **2019**, *119*, DOI: 10.1002/qua.25719.
- (85) Wu, Y.; Ellis, D. E. X-ray absorption near-edge spectra and electronic structure of rhodium compounds. *J. Phys.: Condens. Matter* **1995**, *7*, 3973–3989, DOI: 10.1088/0953-8984/7/20/016.
- (86) Smith, J. W.; Saykally, R. J. Soft X-ray Absorption Spectroscopy of Liquids and Solutions. *Chem. Rev.* **2017**, *117*, 13909–13934, DOI: 10.1021/acs.chemrev.7b00213.
- (87) Gaiduk, A. P.; Galli, G. Local and Global Effects of Dissolved Sodium Chloride on the Structure of Water. *J. Phys. Chem. Lett.* **2017**, *8*, 1496–1502, DOI: 10.1021/acs.jpcllett.7b00239.
- (88) Penfold, T. J.; Curchod, B. F.; Tavernelli, I.; Abela, R.; Rothlisberger, U.; Cherqui, M. Theoretical considerations for the simulation of X-ray absorption spectra: The effect of the solvent for a diplatinum complex. <https://drive.google.com/file/d/182vqPmPJ0f2jYcODWBSv-oHmpwXOP5Ln/view>.

TOC Graphic



Supporting Information:

Solvation effects on halides core spectra with Multilevel Real-Time quantum embedding

Jessica A. Martinez B.,[†] Matteo De Santis,[‡] Michele Pavanello,^{¶,§} Valérie
Vallet,[‡] and André Severo Pereira Gomes^{*,‡}

[†]*Department of Chemistry, Rutgers University, Newark, New Jersey*

[‡]*Univ. Lille, CNRS, UMR 8523 - PhLAM - Physique des Lasers Atomes et Molécules,
F-59000 Lille, France*

[¶]*Department of Physics, Rutgers University, Newark, New Jersey*

[§]*Department of Chemistry, Rutgers University, Newark, New Jersey*

E-mail: andre.gomes@univ-lille.fr

1 Additional Tables and Figures

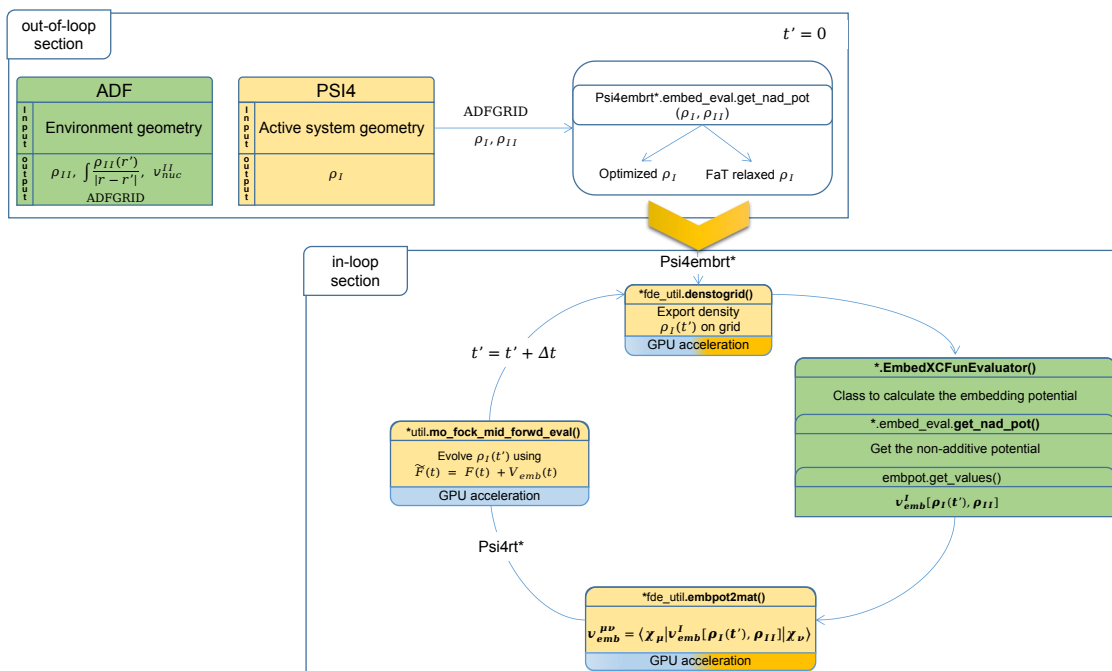


Figure S1: Working flowchart of the $uFDE$ - rt - $TDDFT$ implementation as part of PyBertha package. We offload matrix operations to GPUs, by employing two frameworks, PyTorch and TensorFlow. We called “full” implementation when replacing Numpy operations for tensor operations of two crucial PyBertha functions (namely *embpot2mat.py* and *denstogrid.py* from the *psi4embt.py* module) and all the sub-functions of *util.py* (including *mo_fock_mid_forwd_eval.py*) from the *psi4rt.py* module (Indicated by the blue color). While the “partial” implementation involves replacing the Numpy operations of only two crucial PyBertha functions, indicated by the orange color. Details of the description of the $uFDE$ - rt - $TDDFT$ implementation can be found in^{S1}

References

- (S1) De Santis, M.; Belpassi, L.; Jacob, C. R.; Severo Pereira Gomes, A.; Tarantelli, F.; Visscher, L.; Storchi, L. Environmental Effects with Frozen-Density Embedding in Real-Time Time-Dependent Density Functional Theory Using Localized Basis Functions. *J. Chem. Theory Comput.* **2020**, *16*, 5695–5711, DOI: 10.1021/acs.jctc.0c00603.

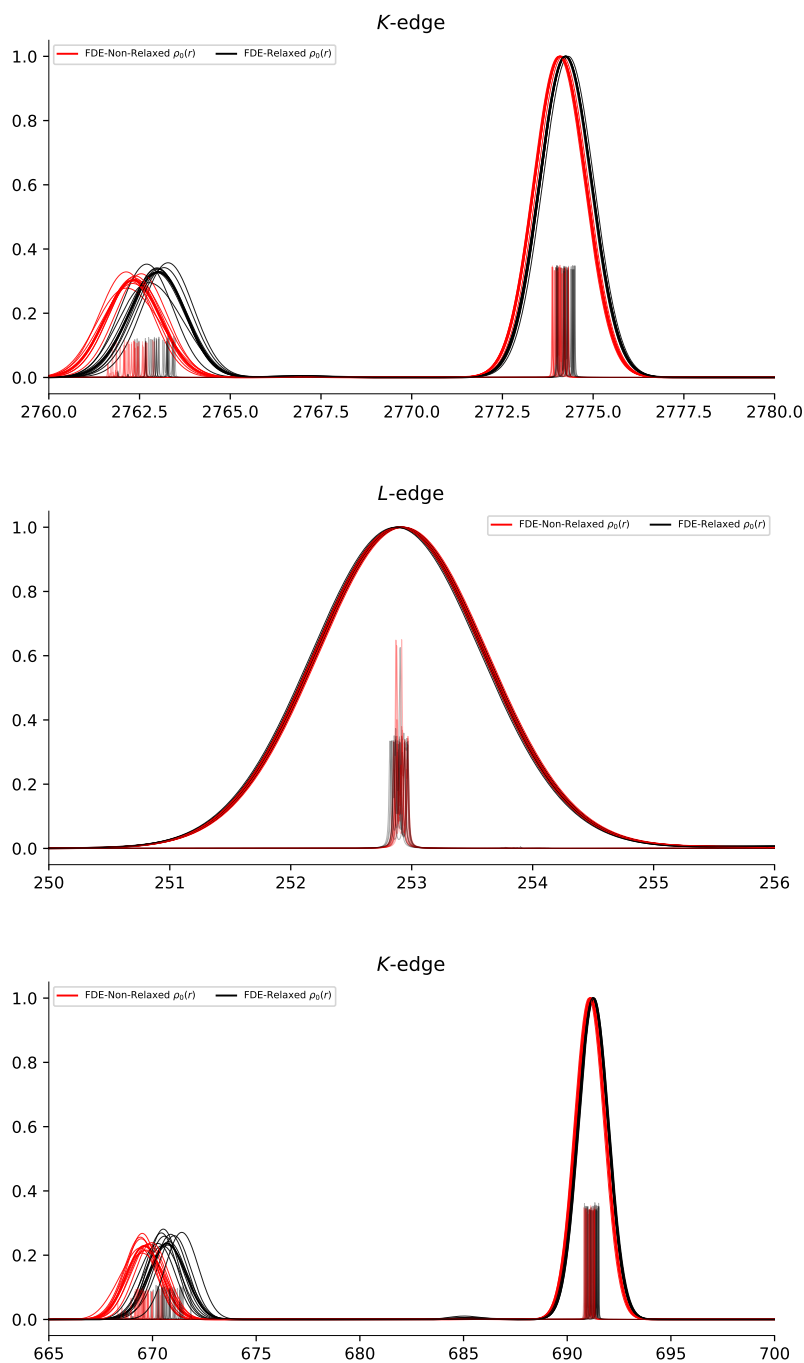


Figure S2: Chloride K-edge (top) and L_1 -edge (middle) and fluoride K-edge (bottom) X-ray absorption spectra for the anions embedded in their first solvation shell (8 water molecules) between the energy range of the free ion edge peak and up to 20 eV (Cl K-edge), 14 eV (Cl L_1 -edge), and 35 eV (F K-edge). Data was obtained by employing FDE-rt-TDDFT with a non-relax and relaxed initial density $\rho(r)$. Inset pictures show the contribution per snapshot and the peaks per excitation. A Gaussian broadening ($\sigma = 0.7$ eV) was used.

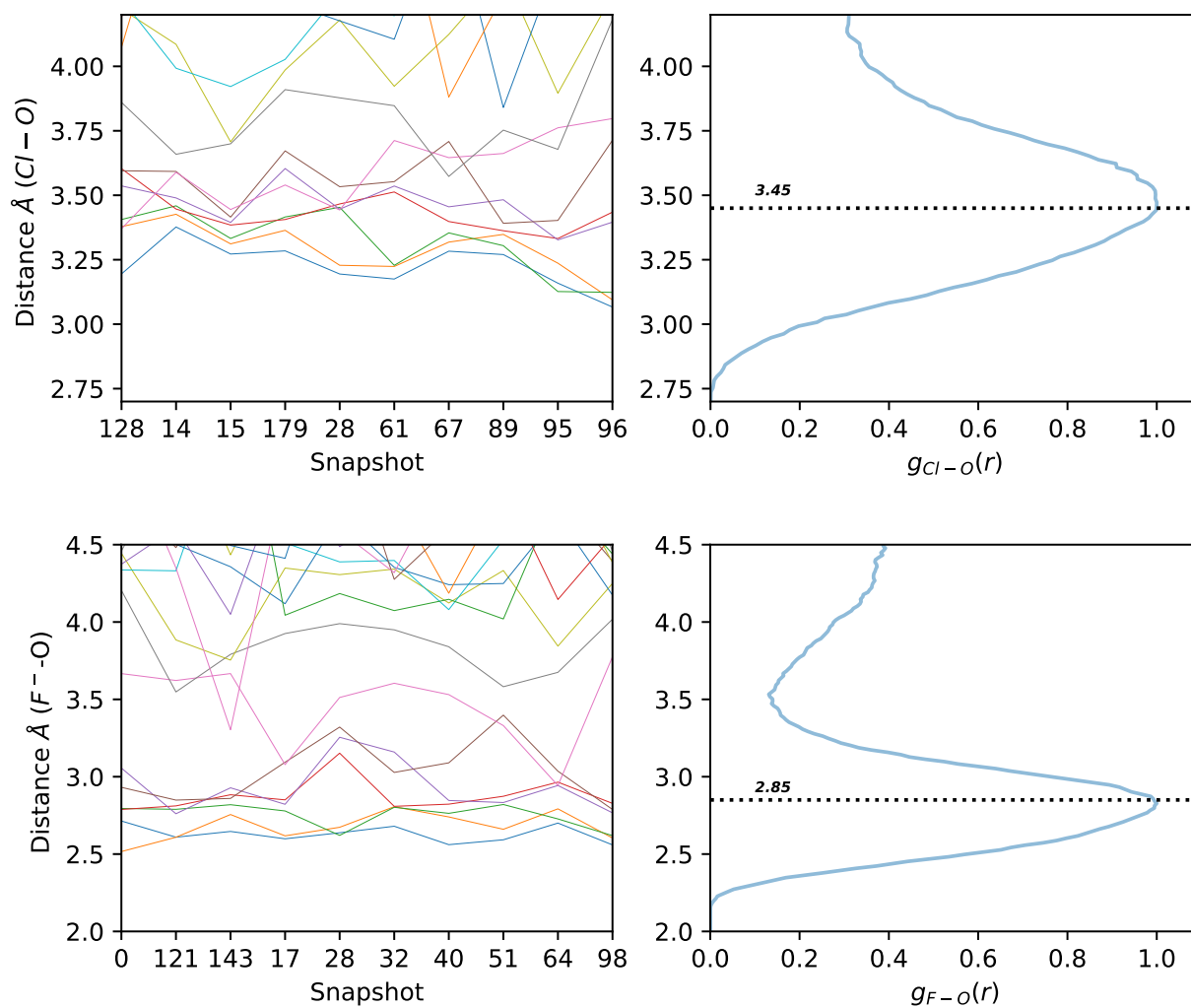


Figure S3: Radial distribution function of the chloride (top) and fluoride(bottom) with respect to the surrounding water molecules among all the 10 selected snapshots.

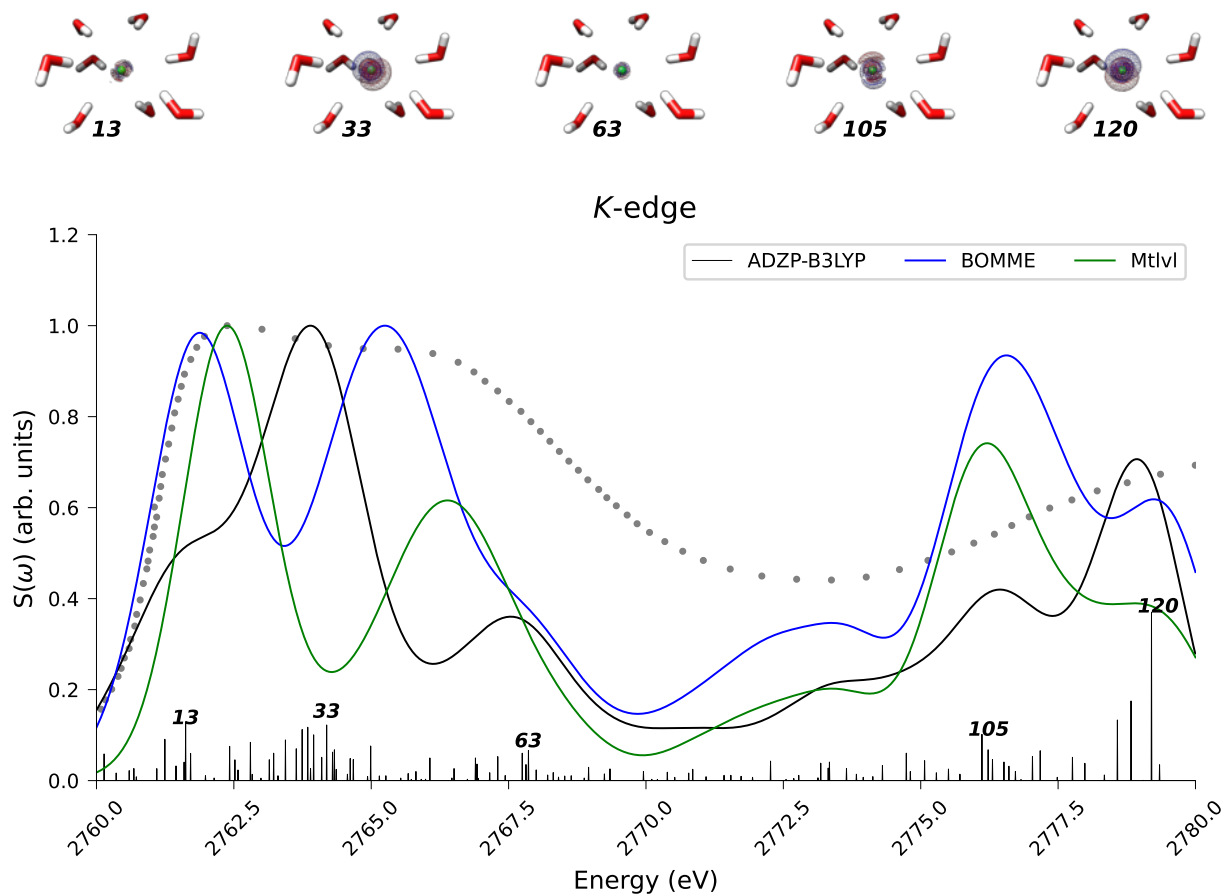


Figure S4: Transition density (TD) analysis for the K-edge X-ray absorption spectra for chloride anion embedded in its first solvation shell (8 water molecules) for BOMME and up to 50 water molecules for ML between the energy range of the free ion edge peak and up to 20 eV. A Gaussian broadening ($\sigma = 0.7$ eV) was used. Top: Transition densities of the corresponding roots displayed with isodensity values of 10^{-6} . Bottom: The halide atom basis is ‘aug-cc-PVDZ’ while for hydrogen and oxygen, we employed ADZP basis set and the B3LYP exchange-correlation functional.

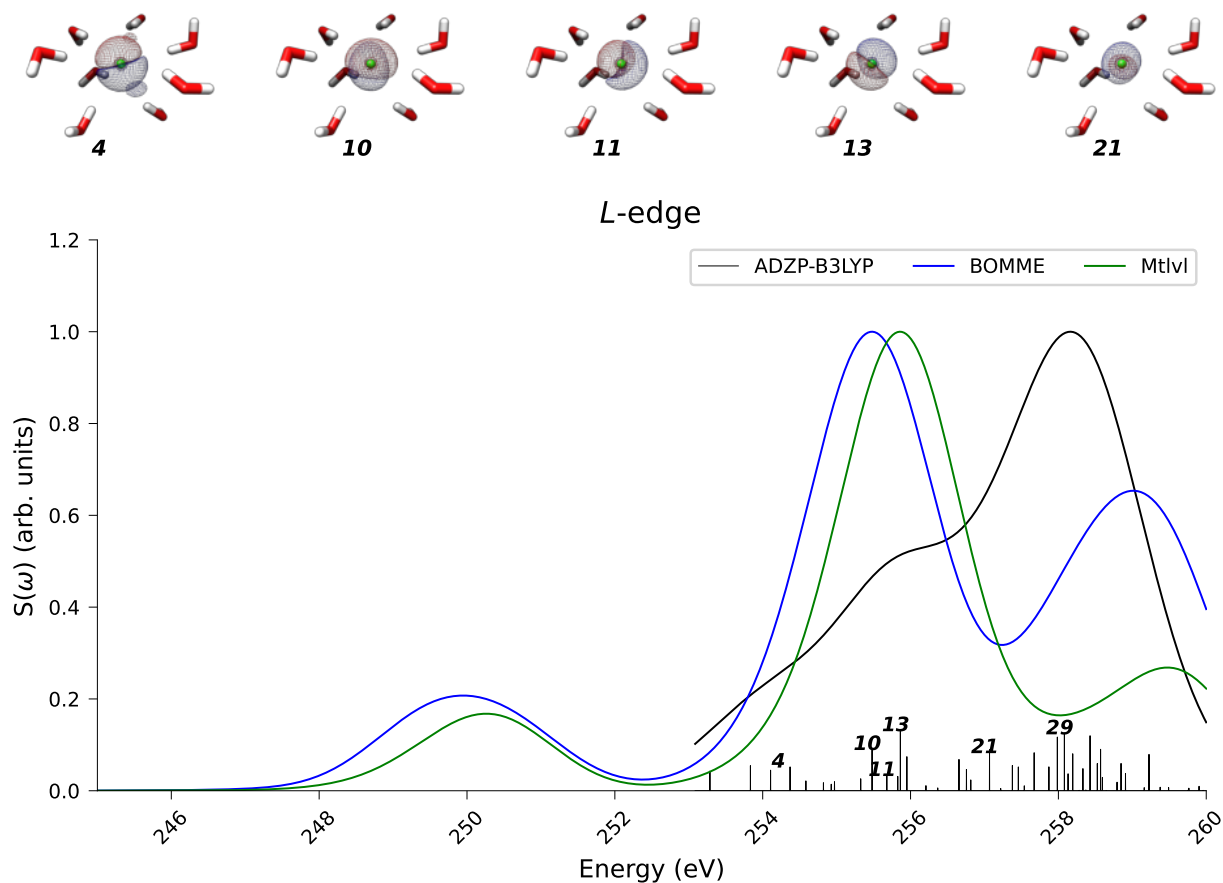


Figure S5: Transition density (TD) analysis for the L_1 -edge X-ray absorption spectra for chloride anion embedded in its first solvation shell (8 water molecules) for BOMME and up to 50 water molecules for ML between the energy range of the free ion edge peak and up to 15 eV. A Gaussian broadening ($\sigma = 0.7$ eV) was used. Top: Transition densities of the corresponding roots displayed with isodensity values of 10^{-6} . Bottom: The halide atom basis is ‘aug-cc-PVDZ’ while for hydrogen and oxygen, we employed ADZP basis set and the B3LYP exchange-correlation functional.

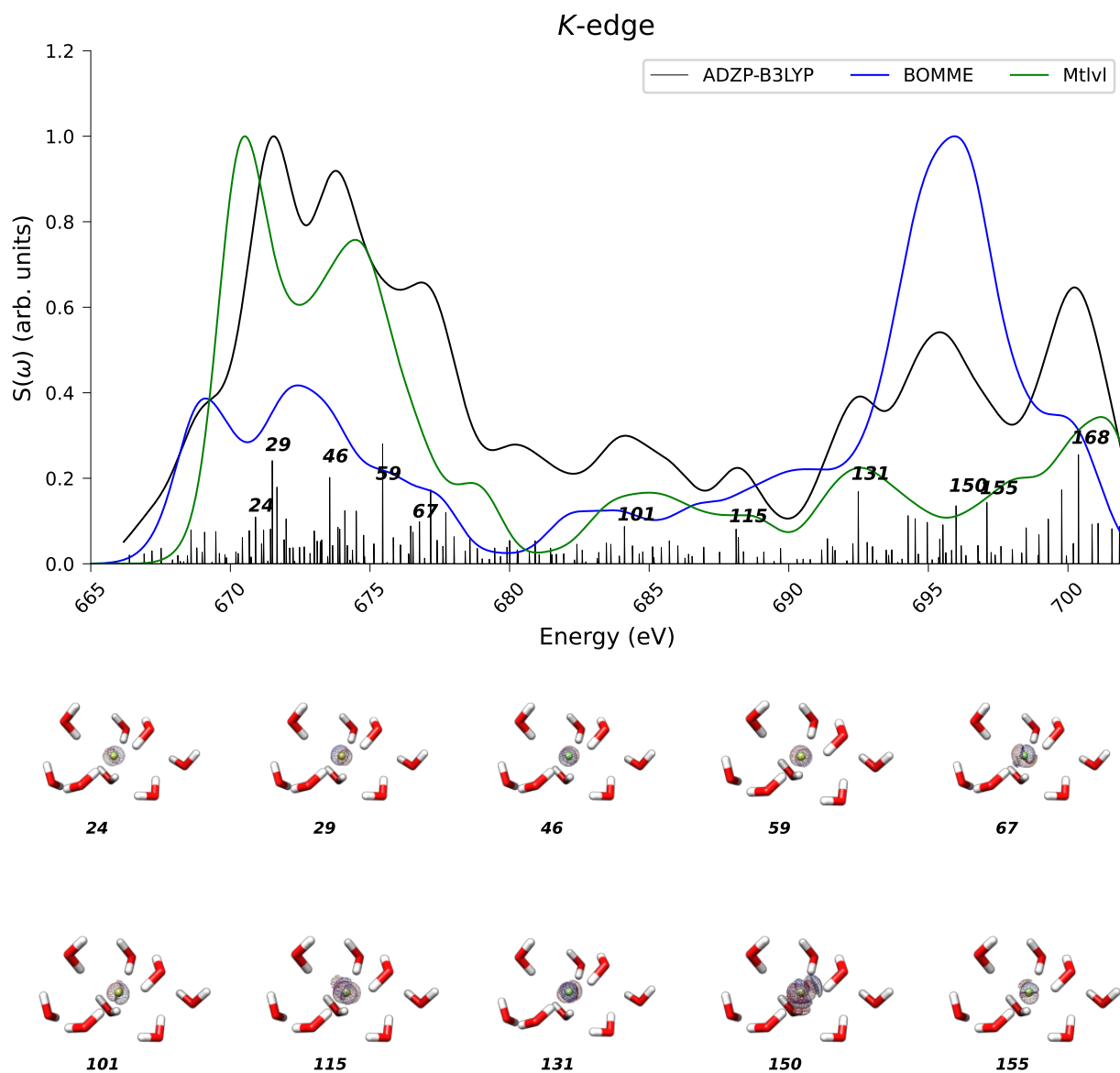


Figure S6: Transition density (TD) analysis for the K-edge X-ray absorption spectra for fluoride anion embedded in its first solvation shell (8 water molecules) for BOMME and up to 50 water molecules for ML between the energy range of the free ion edge peak and up to 35 eV. A Gaussian broadening ($\sigma = 0.7$ eV) was used. Top: Transition densities of the corresponding roots displayed with isodensity values of 10^{-6} . Bottom: The halide atom basis is ‘aug-cc-PVDZ’ while for hydrogen and oxygen, we employed ADZP basis set and the B3LYP exchange-correlation functional.

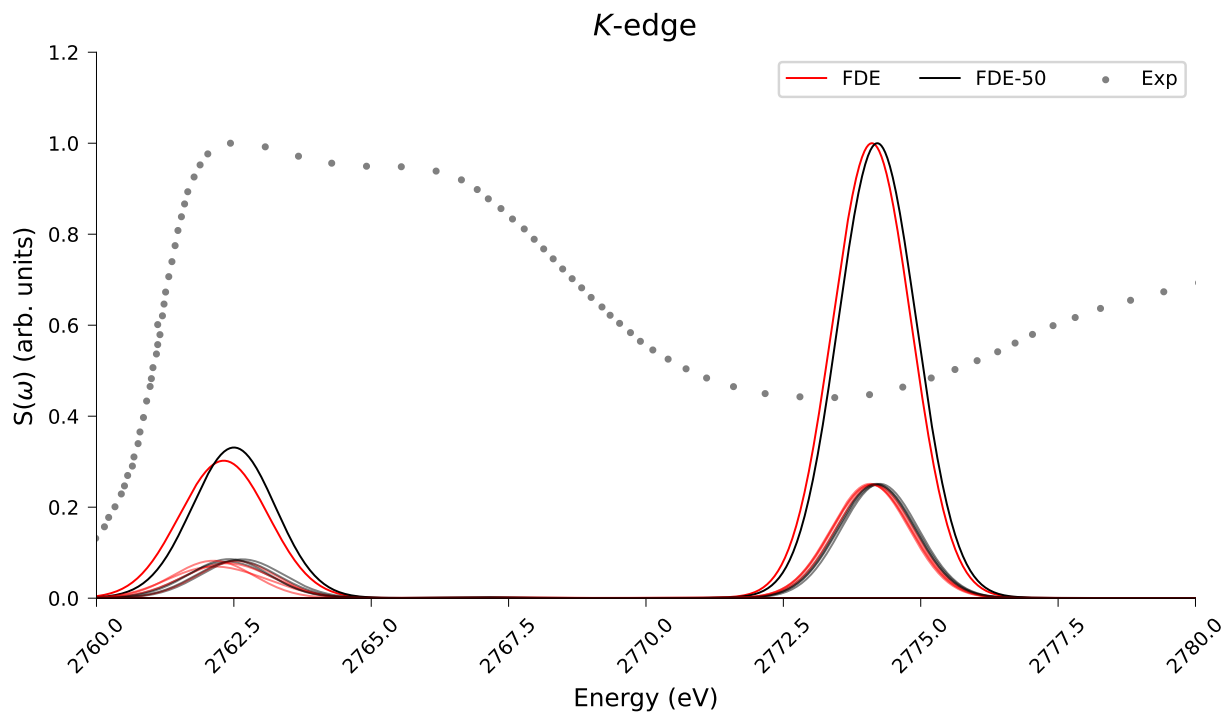


Figure S7: K-edge X-ray absorption spectra for chloride anion embedded in its first solvation shell (8 water molecules) and up to 50 water molecules between the energy range of the free ion edge peak and up to 20 eV. Data was obtained by employing FDE-rt-TDDFT with a non-relax and relaxed initial density $\rho(r)$. 5 cycles of Freeze and Thaw were employed to obtain a relaxed initial density. Inset pictures show the contribution per snapshot. A Gaussian broadening ($\sigma = 0.7$ eV) was used.

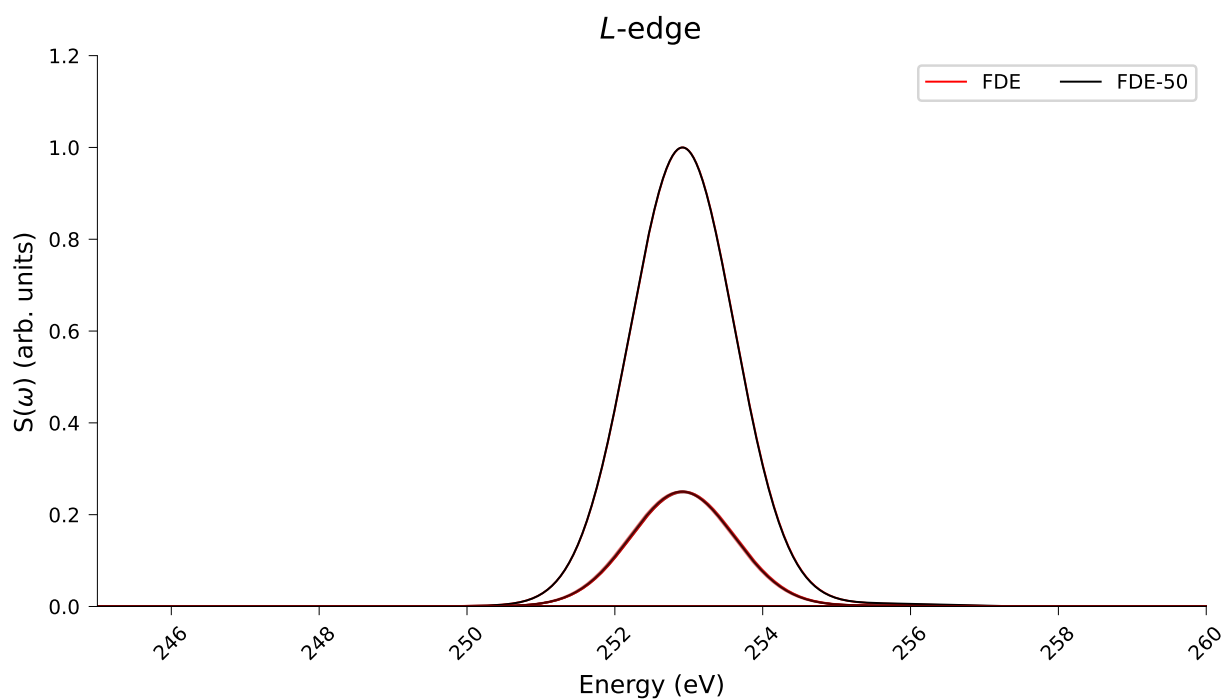


Figure S8: L_1 -edge X-ray absorption spectra for chloride anion embedded in its first solvation shell (8 water molecules) and up to 50 water molecules between the energy range of the free ion edge peak and up to 15 eV. Data was obtained by employing FDE-rt-TDDFT with a non-relax and relaxed initial density $\rho(r)$. 5 cycles of Freeze and Thaw were employed to obtain a relaxed initial density. Inset pictures show the contribution per snapshot. A Gaussian broadening ($\sigma = 0.7$ eV) was used.

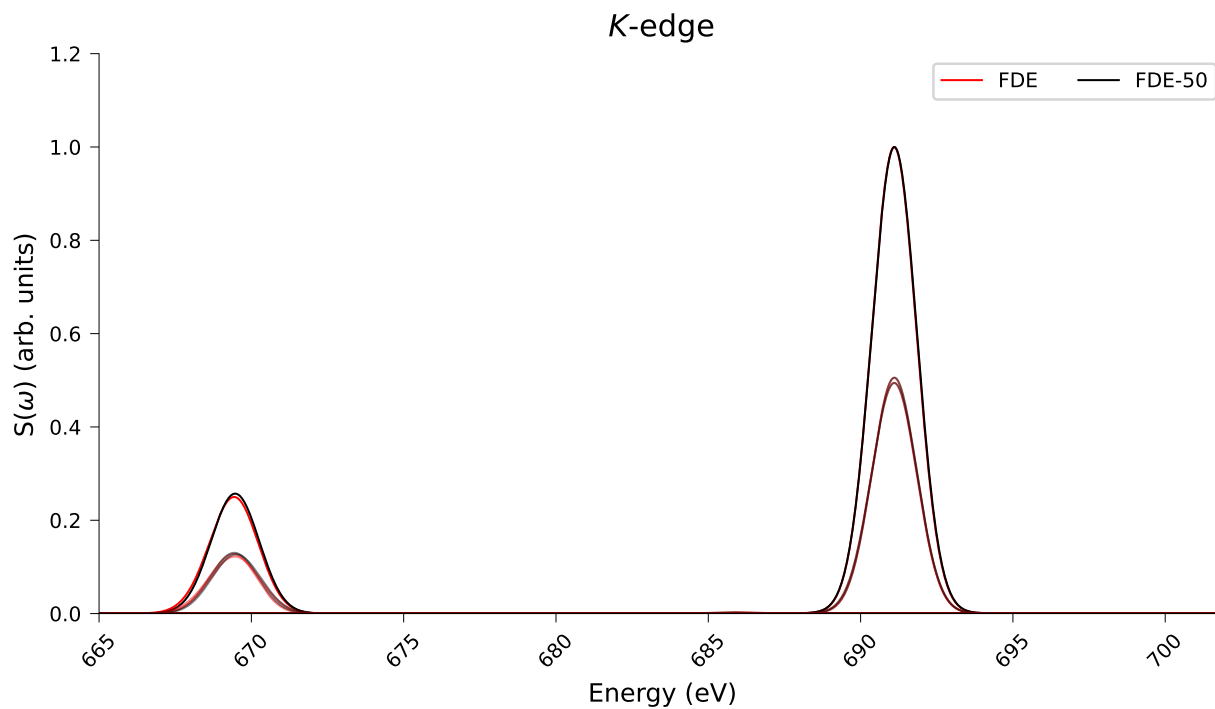


Figure S9: K-edge X-ray absorption spectra for fluoride anion embedded in its first solvation shell (8 water molecules) and up to 50 water molecules between the energy range of the free ion edge peak and up to 35 eV. Data was obtained by employing FDE-rt-TDDFT with a non-relax and relaxed initial density $\rho(r)$. 5 cycles of Freeze and Thaw were employed to obtain a relaxed initial density. Inset pictures show the contribution per snapshot. A Gaussian broadening ($\sigma = 0.7$ eV) was used.

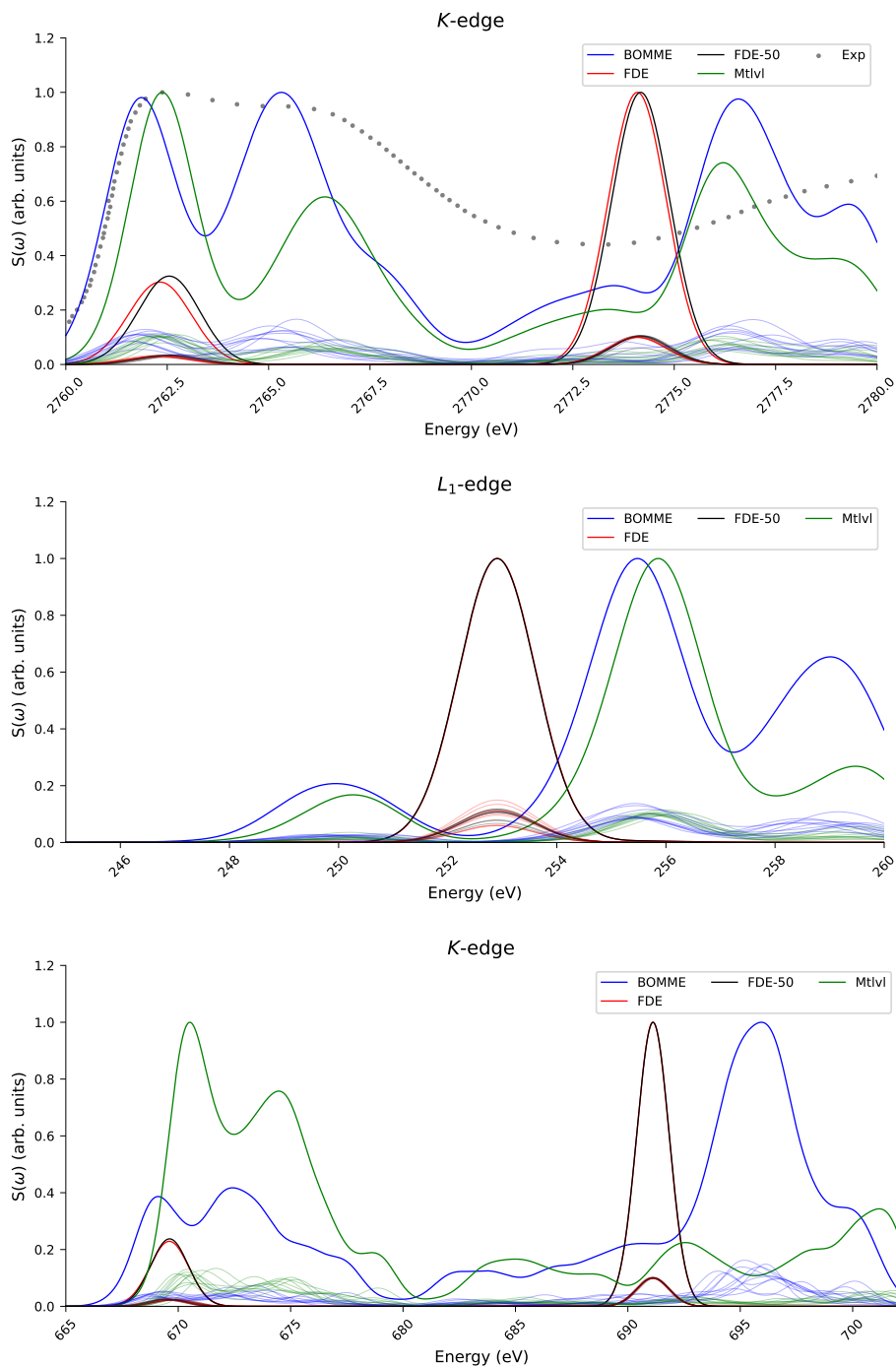


Figure S10: Chloride K-edge (top) and L₁-edge (middle) and fluoride K-edge (bottom) X-ray absorption spectra for the anions embedded in their first solvation shell (8 water molecules) between the energy range of the free ion edge peak and up to 20 eV (Cl K-edge), 14 eV (Cl L₁-edge), and 25 eV (F K-edge). Data was obtained by employing FDE-rt-TDDFT (FDE) up to 8 water, and up to 50 waters (FDE-50), BOMME-rt-TDDFT(BOMME), and ML-rt-TDDFT methods. Inset pictures show the contribution per snapshot and the peaks per excitation. A Gaussian broadening ($\sigma = 0.7$ eV) was used.